Retrograde mitochondrial signaling governs the identity and maturity of metabolic tissues

Gemma L. Pearson[1*]; Emily M. Walker[1*]; Nathan Lawlor[2]; Anne Lietzke[1]; Vaibhav Sidarala[1]; Jie Zhu[1]; Tracy Stromer[1]; Emma C. Reck[1]; Aaron Renberg[1]; Kawthar Mohamed[1]; Vishal S. Parekh[3]; Irina X. Zhang[3]; Benjamin Thompson[3]; Deqiang Zhang[4]; Sarah A. Duplaga[5]; Leena Haataja[1]; Stephen C.J. Parker[6]; Peter Arvan[1]; Lei Yin[4]; Brett A. Kaufman[5]; Leslie S. Satin[3]; Lori Sussel[7]; Michael L. Stitzel[2]; and Scott A. Soleimanpour[1,4,8]

[1]Division of Metabolism, Endocrinology & Diabetes and Department of Internal Medicine, University of Michigan, Ann Arbor, MI, USA.

[2]The Jackson Laboratory for Genomic Medicine, Farmington, CT, USA.

[3]Department of Pharmacology, University of Michigan, Ann Arbor, MI, USA

[4]Department of Molecular and Integrative Physiology, University of Michigan, Ann Arbor, MI, USA

[5]Vascular Medicine Institute, Division of Cardiology, Department of Medicine, University of Pittsburgh School of Medicine, Pittsburgh, PA, USA

[6]Department of Computational Medicine and Bioinformatics, University of Michigan, Ann Arbor, MI, USA

[7]Barbara Davis Center for Diabetes, Department of Pediatrics, University of Colorado Anschutz Medical Campus, Aurora, CO, USA

[8]VA Ann Arbor Healthcare System, Ann Arbor, MI, USA.

*These authors contributed equally to this work

Corresponding Author

Scott A. Soleimanpour, MD, 1000 Wall Street, Brehm Tower Room 6329, Ann Arbor, MI 48105, USA. Phone: (734) 763-0528 E-mail: ssol@med.umich.edu

ABSTRACT

Mitochondrial dysfunction is a hallmark of metabolic diseases, including diabetes, yet the downstream consequences of mitochondrial damage in metabolic tissues are often unclear. Here, we report that mitochondrial dysfunction engages a retrograde signaling program that impairs cellular identity and maturity across many metabolic tissues. Impairments in the mitochondrial quality control machinery, which we observe in pancreatic β cells of humans with diabetes, cause reductions of β cell mass, surprisingly due to β cell dedifferentiation, rather than apoptosis. Utilizing transcriptomic profiling, lineage tracing, and assessments of chromatin accessibility, we find that targeted defects anywhere in the mitochondrial quality control pathway (genome integrity, dynamics, or turnover) activate the mitochondrial integrated stress response and promote cellular immaturity in β cells, hepatocytes, and brown adipocytes. Intriguingly, pharmacologic blockade of mitochondrial retrograde signals restores β cell mass and identity to ameliorate hyperglycemia following mitochondrial damage. Thus, we observe that a shared mitochondrial retrograde response controls cellular identity across metabolic tissues, which could be a promising target to treat or prevent metabolic diseases.

INTRODUCTION

Mitochondria are vital to cellular bioenergetics in eukaryotes, with highly visible impacts of mitochondria within mammalian metabolic tissues. Indeed, mitochondrial defects occur in numerous tissues that are critical to the development of metabolic diseases, such as type 2 diabetes (T2D) [1]. Insulin-producing pancreatic β cells from islet donors with T2D have dysmorphic mitochondrial ultrastructure as well as reductions in the ratio of ATP/ADP following glucose stimulation [2,3]. Skeletal muscle from individuals with T2D have impaired mitochondrial ATP production in response to insulin, reduced mitochondrial respiratory capacity, and decreased mitochondrial (mt)DNA content [4-7]. Further, hepatic mitochondrial uncoupling and proton leak in T2D patients results in decreases in mitochondrial respiration as well as ATP synthesis and turnover [8-11].

Since Lowell and Shulman proposed that mitochondrial dysfunction provides a unifying hypothesis for T2D development, features of mitochondrial impairment have also been described in myocardium, vascular endothelium, adipose tissue, and the central and peripheral nervous system [1,12]. Importantly, the impact of mitochondrial dysfunction in T2D pathogenesis has been bolstered by recent work determining that β cell mitochondrial defects precede the development of T2D in humans [13]. Moreover, several human genetic studies support links between mitochondria and T2D [14-19].

Loss of terminal cell identity has been recently observed in several tissues in metabolic diseases. Whereas the maintenance of pancreatic β cell mass was previously believed to solely depend on a balance of β cell replication and apoptosis [20], the loss of β cell differentiation or identity is a key factor driving β cell failure in T2D [21-23]. Dedifferentiated or immature β cells lack factors important in fully mature adult β cells, may acquire endocrine progenitor markers, and often express other islet cell hormones [21-23]. Impairments in differentiation have also been observed in other metabolic tissues during T2D [24-26]. Despite the central importance of

mitochondrial dysfunction to T2D, the question if mitochondrial dysfunction directly promotes dedifferentiation or immaturity in metabolic tissues has been unaddressed.

Here, we find that mitochondrial dysfunction engages a retrograde signaling program that promotes immaturity in metabolic tissues. Utilizing multiple independent mouse genetic models, lineage tracing approaches, biochemical and metabolic assays, as well as transcriptomic profiling, we observe that loss of mitochondrial quality control elicits dedifferentiation in pancreatic β cells, ultimately leading to loss of β cell mass and hyperglycemia. Importantly, we find that mitochondrial dysfunction yields a shared signature including loss of terminal maturity markers, induction of progenitor markers, and activation of the mitochondrial integrated stress response (ISR) in multiple metabolic tissues via complementary analysis of genetic mouse models in β cells, hepatocytes, brown adipocytes, as well as in primary human islets. Further, mitochondrial dysfunction induces chromatin remodeling consistent with the loss of terminal cell identity and the activation of the ISR. Inhibition of the ISR *in vivo* restores β cell mass and maturity and ameliorated glucose intolerance following mitochondrial dysfunction, illustrating that induction of retrograde signaling directly promotes dedifferentiation of key metabolic tissues that may be essential to the development of metabolic diseases.

RESULTS

Mitochondrial quality control is impaired in β-cells in T2D

Abnormalities in mitochondrial structure and function have been implicated in several metabolic tissues in T2D, including pancreatic β-cells [2,3]. Defects in mitochondrial structure and function intimate that mitochondrial defects in T2D may arise due to impairments in mitochondrial quality control or the mitochondrial life cycle, which tightly regulate mitochondrial genome integrity, biogenesis, mitochondrial dynamics, and turnover by mitophagy [27,28]. As β-cell failure underlies the development of T2D, we investigated whether there is evidence of impaired mitochondrial quality control in human islets from T2D donors. We first observed that human islets

from T2D donors develop significant reductions in mtDNA content compared to non-diabetic donors (Figure 1A). Concordantly, we found significantly reduced expression of 11 of the 13 mitochondrially encoded RNAs (mtRNA) by single cell RNA sequencing in β-cells of T2D donors (Figure 1B). Importantly, there was no differences in mtRNA levels in α-cells or other non β-cells in T2D (Figure S1A and [29]), indicating a β-cell specific defect in mitochondrial genome integrity. We also did not observe differences in functional mitochondrial mass between non-diabetic and T2D β cells, suggesting that reductions in mtDNA content are not secondary to reduced mitochondrial mass (data not shown). As published ultrastructural studies have previously indicated defects in mitochondrial architecture in T2D indicative of alterations in mitochondrial dynamics [2,3], we next proceeded to evaluate mitochondrial turnover. To determine if mitophagy, or selective mitochondrial autophagy, was altered in β-cells from T2D donors, we analyzed mitophagic flux in single cells by flow cytometry analysis as per our previous approaches [30-32]. In β-cells from non-diabetic donors, we observed the expected increase in mitophagic flux, defined by cells with increases in depolarized mitochondria within the acidic lysosome compartment, following exposure to the potassium ionophore valinomycin, a known stimulator of mitophagy (Figures 1C). Interestingly, T2D β cells exhibited lower mitophagic flux following valinomycin exposure, consistent with impairments in mitophagy (Figure 1C). Notably, defects in mitophagy were not observed in non-β cells from T2D donors (Figure 1D), again in line with a β-cell specific defect in T2D. Taken together, these results indicate that β cells in T2D develop specific defects in mtDNA content, mtRNA levels, mitochondrial structure, and mitophagy, consistent with comprehensive impairments in mitochondrial quality control.

To determine whether changes in β-cell mitochondrial quality control in T2D are secondary to obesity, we measured mtDNA content and mitophagy in transgenic mice expressing the mt-Keima pH sensitive mitophagy reporter [33,34] fed a regular fat diet (RFD) or high fat diet (HFD) for up to one year of age (Figure S1D). Notably, we observed that no significant differences in islet mtDNA content secondary to age or diet (Figure S1D). We did observe a small, yet significant

reduction in rates of mitophagy in β-cells following diet-induced obesity that were not observed in non-β-cells by flow cytometry (Figure S1E-F). Thus, the slight reductions in mitophagy, yet not mtDNA content, following HFD suggests the peripheral effects of obesity or insulin resistance alone do not account for changes in β-cell mitochondrial quality control observed in T2D and instead suggest an intrinsic defect in β-cells that may be relevant for T2D.

Mitochondrial quality control is necessary to maintain β-cell mass and function

To directly ascertain if impairment of mitochondrial quality control leads to progressive β-cell failure similar to what is observed in T2D, we generated several mouse genetic models bearing deficiency of components of the mitochondrial quality control machinery, initially targeting mitophagy and mitochondrial genome integrity. We first generated mice bearing β-cell specific deletion of Clec16a, a critical regulator of mitophagy (*Clec16a*$^{f/f}$; *Ins1*-Cre, hereafter known as β-Clec16a^{KO}; Figure 1E). Notably, expression of *Clec16a* is reduced in islets of T2D donors, and *Clec16a* is also a direct transcriptional target of the T2D gene *Pdx1* [35,36]. β-Clec16a^{KO} mice as well as controls were then fed RFD or HFD for 12 weeks prior to physiologic or morphometric assays, and we did not observe differences in insulin sensitivity between controls and β-Clec16a^{KO} mice under RFD or HFD (data not shown). Of note, *Ins1*-Cre and floxed alone controls were phenotypically indistinguishable from each other, exhibiting no differences in glucose tolerance or body weight and were pooled as controls for subsequent analyses, consistent with previous studies from our group and others [31,37]. β-Clec16a^{KO} mice developed glucose intolerance as expected in RFD-fed mice, which was then markedly exacerbated following diet-induced obesity (DIO; Figure 1F). β-Clec16a^{KO} animals also had reductions in serum insulin concentrations upon HFD as well as decreased insulin secretion *in vivo* (Figures 1G-H).

We next evaluated β-cell mass in mitophagy-deficient mice and observed that β-Clec16a^{KO} animals failed to expand their β-cell mass to compensate for diet-induced insulin resistance (Figure 1I). We did not observe differences in α-cell mass between the groups (Figure

S2A). To understand the etiology of reduced β-cell mass in HFD-fed β-Clec16a^{KO} mice, we assessed markers of β-cell proliferation and apoptosis. While β-cell mitochondrial dysfunction is primarily associated with defects in cell replication or survival, we observed a trend toward increased β-cell replication (Figure S2B) and no changes in survival in HFD-fed β-Clec16a^{KO} mice (Figure 1J), which could not explain the loss of β-cell mass we observed.

As aging is also a risk factor for the development of T2D [38], we evaluated β-Clec16a^{KO} mice up to one year of age. We also noted that mitophagy-deficiency led to severe glucose intolerance and reduced β-cell mass with age, similar to what we observed in HFD-fed β-Clec16a^{KO} animals (Figures S2C-F). To ensure the physiologic and histologic changes we observed were not attributable to developmental defects, we next generated inducible β-cell specific Clec16a knockout animals by intercrossing our mice bearing the Clec16a conditional allele with the tamoxifen-inducible MIP-CreERT strain (*Clec16a*$^{f/f}$; *MIP*-CreERT, hereafter known as iβ-Clec16a^{KO} mice). Following tamoxifen-mediated recombination, we observed that iβ-Clec16a^{KO} mice phenocopied our observations in constitutive β-cell Clec16a knockouts, with mild glucose intolerance on RFD, exacerbations in glucose intolerance upon HFD, reductions in β-cell mass on HFD, and no differences in β-cell replication or survival (Figures S2G-J). Thus, mitophagy is vital for the preservation of β-cell mass following aging or obesity independent of control of cell replication or survival or defects in β-cell development.

Next, we generated mice bearing reductions of mtDNA content following loss of Tfam, a master regulator of mtDNA copy number control, by intercrossing *Ins1*-Cre and *Tfam*$^{f/f}$ mice (hereafter noted as β-Tfam^{KO}; Figure 1K). Specifically, we bred *Tfam*$^{f/f}$ mice to the highly specific *Ins1-Cre* knockin strain to alleviate concerns related to the transgenic *RIP2*-Cre strain previously employed to knockout Tfam [39,40]. We first observed the expected reductions of mtDNA in β-Tfam^{KO} islets (Figures S2K). To confirm that mtDNA depletion was specific to β-cells, we additionally intercrossed β-Tfam^{KO} mice with the ROSA26-lox-STOP-lox-tdTomato reporter strain, such that β-cells are irreversibly labeled with the tdTomato reporter following Cre-mediated recombination

[41]. Following fluorescence-activated cell sorting of tdTomato positive β-cells, we observed near complete depletion of mtDNA content in β-Tfam^{KO} mice, while tdTomato negative cells were unaffected (Figure 1L). Similar to Clec16a-deficient mice, β-Tfam^{KO} mice had progressive glucose intolerance with age, decreased insulin secretion following glucose administration, and markedly reduced β-cell mass without changes in α-cell mass (Figures 1M-O, S2L-N). Interestingly, β-Tfam^{KO} mice had an additional significant increase in β-cell replication with a small increase in apoptosis (Figures 1P-Q), which might be expected to favor an increase or at least no differences in β-cell mass. Similar to Clec16a-deficient mice, these results suggest that loss of Tfam markedly reduces β-cell mass and are unlikely to be reconciled only by control of β-cell replication or survival. Further, these models implicate that defects in mitochondrial quality control lead to progressive loss of β-cell mass and function similar to what is observed in T2D.

Defects in mitochondrial quality control induce loss of β-cell identity

Given the unclear etiology of β-cell failure following distinct approaches to impair mitochondrial quality control, we explored possible shared mechanistic explanations for the similarities in phenotypic responses. To begin to uncover these underlying mechanisms, we initially performed high-throughput RNA sequencing (RNAseq) on isolated islets from RFD and HFD-treated β-*Clec16a*^{KO} mice as well as β-Tfam^{KO} mice and their respective controls. Gene set enrichment analysis (GSEA) were then used to determine if Clec16a- or Tfam-deficient β-cells exhibited changes in β-cell maturity/immaturity, overlaying our results with a previously validated β-cell maturity/immaturity gene set [42]. Importantly, GSEA revealed significant upregulation of genes associated with β-cell immaturity with corresponding downregulation of genes associated with mature β-cells in both RFD and HFD-fed β-Clec16a^{KO} as well as β-Tfam^{KO} islets (Figures 3A-D). Notably, pathway analysis identified specific divergences in control and β-Clec16a^{KO} islets that were exacerbated with HFD. Clec16a-deficient islets displayed downregulation of genes related to insulin secretion and mitochondrial lipid metabolism (β-oxidation and mitochondrial long

chain fatty acid oxidation), suggestive of maladaptive β-cell metabolic function. Clec16a-deficient islets also demonstrated increased enrichment for developmental or morphogenetic pathways, including Notch and Id signaling pathways (Figures S3A-B; [43-46]). Similarly, pathway analysis of β-Tfam^{KO} islets displayed downregulation of insulin secretion and key β-cell signature pathways (insulin secretion, maturity onset diabetes of the young, and type II diabetes mellitus) when compared to controls (Figure S4A). Moreover, core β-cell maturity/identity markers, including *Ins2*, *Ucn3*, *Glut2*, and *MafA*, were all significantly reduced following mtDNA depletion or impaired mitophagy (Figures 2E-F). Reductions of core β-cell maturity markers were also found after analyzing gene expression data from an additional recently described model of impaired mitochondrial quality control by loss of mitochondrial fusion following deletion of both Mitofusins 1 and 2 in β-cells (also known β-Mfn1/2^{DKO} mice; Figure S4B; [31]). Notably, loss of Mfn1/2 also has been found to lead to reductions in β-cell mass with age [47]. Stem cell or early endocrine progenitor cell markers such as *Oct4*, *Sox2*, *Nanog*, and *Ngn3* were not upregulated in β-Clec16a^{KO}, β-Tfam^{KO}, or β-Mfn1/2^{DKO} islets (data not shown), indicating loss of mitochondrial quality control induces markers of immaturity and loss of terminal β-cell identity without a signature associated with regression to early developmental precursors.

To verify changes in β-cell maturity, we performed immunostaining on pancreatic sections from models of impaired mitochondrial quality control. The dedifferentiation marker Aldh1a3, which is not observed in terminally differentiated β-cells and has been found in islets in T2D [21,48], was detectable in RFD-fed β-Clec16a^{KO} mice and further increased in both HFD or aged β-Clec16a^{KO} mice (Figures 2G and S5A). Aldh1a3 was also upregulated in β-Tfam^{KO}, iβ-Clec16a^{KO}, and β-Mfn1/2^{DKO} β-cells (Figures 2J, S5B-C). Further, key β-cell maturation markers Glut2 and Ucn3 were markedly decreased in all models of impaired mitochondrial quality control (Figures 2H-I, 2K, S5D-G).

We next employed genetic lineage tracing to confirm the loss of β-cell identity in Clec16a and Tfam-deficient mice. As noted above, both β-*Clec16a*^{KO} and β-Tfam^{KO} mice (and *Ins1-Cre*

control littermates) were intercrossed with the ROSA26-lox-STOP-lox-tdTomato reporter strain [41], such that β-cells were irreversibly labeled with the tdTomato reporter following Cre-mediated recombination. By this lineage tracing strategy, a loss of β-cell identity would thus lead to an increased number of insulin negative, tdTomato positive cells. As expected, >95% of β-cells were marked by double positivity for insulin and tdTomato in *Ins1*-Cre control mice, consistent with previous reports (data not shown and [37]). No changes in tdTomato lineage allocation were observed between RFD-fed β-*Clec16a*^{KO} mice and controls. Interestingly, HFD-fed β-*Clec16a*^{KO} mice had significantly more insulin-negative tdTomato-positive cells compared to HFD controls (Figures 3A-D). We also observed a robust increase in insulin-negative tdTomato-positive cells in Tfam-deficient mice compared to controls (Figures 3F-H), suggesting a profound impact of mitochondrial quality control on β-cell identity. Surprisingly, we also observed a trend towards an increase in glucagon-positive, tdTomato positive cells in HFD-fed β-*Clec16a*^{KO} mice that was significantly increased in β-Tfam^{KO} mice which could signify changes in β-cell fate (Figures 3E, 3I). These complementary studies, in several independent models resembling mitochondrial dysfunction in T2D, all confirm that mitochondrial quality control is essential to maintain β-cell identity.

Defective mitochondrial quality control induces the integrated stress response (ISR)

We observe that unique defects in mitochondrial quality control all lead to a shared endpoint of loss of β-cell mass and identity. This led us to hypothesize that impairments in mitochondrial quality control induce a common mitochondrial-nuclear signaling circuit leading to a transcriptional response consistent with β-cell dedifferentiation/immaturity. To determine if a common transcriptional signature is elicited by mitochondrial dysfunction, we performed a comparative analysis of the top 500 up- and down-regulated genes by RNAseq across our models of mitophagy deficiency (β-Clec16a^{KO}), mtDNA depletion (β-Tfam^{KO}) and defective fusion (β-Mfn1/2^{DKO}). Interestingly, we found 62 upregulated and 29 downregulated genes in common

across all three models (Figures 4A-B). To search for connections between these targets, we next analyzed these 91 commonly differentially expressed genes by STRING (Search Tool for the Retrieval of Interacting Genes/Proteins; [49]). STRING revealed 2 highly connected nodes following defects in mitochondrial quality control, (1) an expected change in targets related to mitochondrial-encoded transcripts and (2) an unexpected interaction relating to key targets in the β-cell maturity and integrated stress response (ISR) pathways (Figure 4C).

While anterograde signaling to mitochondria has been described in β-cells [35,50], mitochondrial signals that direct nuclear gene expression (retrograde signaling) have not been observed to date. A candidate pathway to mediate mitochondrial retrograde signaling is the ISR, which coalesces mitochondrial or ER damage responses into a coordinated pathway [51], triggered by phosphorylation of the eukaryotic translation initiation factor Eif2α, which then stabilizes Atf4 to promote downstream transcriptional responses. Indeed, Eif2α phosphorylation and Atf4 protein were significantly increased in β-*Clec16a*^{KO} islets (Figure 4D). We also observed upregulation of canonical ISR transcriptional targets in RFD-fed β-Clec16a^{KO} mice, which increased to a greater degree upon HFD (Figure 4E). We similarly observed upregulation of canonical ISR transcriptional targets in β-Tfam^{KO} islets as well as β-Mfn1/2^{DKO} islets (Figures 4F and S4B). In addition, we observed increased expression of *Txnip*, which connects glucotoxicity with mitochondrial damage [52]. To determine if the ISR was activated by mitochondrial or ER damage, we measured expression of *Bip*, a key ER chaperone activated following ER damage but not induced in the mitochondrial ISR [53]. Importantly, we did not observe increases in *Bip* expression in either β-Clec16a^{KO} or β-Tfam^{KO} islets (Figures 5G-H). Moreover, we found no overt changes in ER morphology in RFD or HFD β-Clec16a^{KO} islets (Figure S6A-D) or β-Mfn1/2^{DKO} islets [31] by transmission electron microscopy (TEM), consistent with the induction of the mitochondrial ISR.

To determine if mitochondrial dysfunction elicited the ISR and loss of β-cell maturity in humans, we next generated TFAM-deficient primary human islets using the recently described pseudoislet approach [54]. Briefly, primary human islets were dispersed, transduced with adenoviral

particles encoding shRNA targeting TFAM (or scramble controls), and then re-aggregated into pseudoislets. We first confirmed highly efficient TFAM mRNA and protein knockdown 7 days after human pseudoislet formation (Figures 4I-J). Further, we confirmed a reduction in expression of mtRNAs following shTFAM exposure, consistent with impairments in TFAM function (Figure 4I). Consistent with our observation in mouse models, loss of TFAM activated the mitochondrial ISR in human islets, as we found increases in Eif2α phosphorylation and ATF4 protein, induction of ISR transcriptional targets *TRIB3* and *CEBPβ*, increased *TXNIP* expression, and no alterations in *BIP* expression (Figures 4K-L). Further, we observed evidence of loss of β cell maturity following TFAM deficiency, with decreases in *GLUT1*, *MAFA*, and *PDX1* expression in shTFAM-treated human pseudoislets (Figure 4M). Importantly, these results confirm that defects in mitochondrial quality control induce both β cell immaturity and the ISR in rodent and human islets.

Loss of mitochondrial quality control induces chromatin remodeling

To definitively resolve changes in the transcriptional landscape of β cells following loss of mitochondrial quality control, we applied both single-nuclei RNAseq and ATACseq to assess chromatin remodeling that may be altered by mitochondrial retrograde signaling. UMAP plots of snRNAseq and snATACseq revealed highly distinct populations of β cells of HFD-fed β-Clec16a^{KO} mice compared to controls (Figures 5A). These results were supported by pathway analyses which found significant differences between biological processes in β cells from control and β-Clec16a^{KO} mice (Figures S7A-B). Indeed, snRNAseq results revealed an enriched expression of targets associated with insulin secretion in control β cells when compared to Clec16a-deficient β cells (Figures S7A-B). An analysis of snATACseq data revealed >25,000 de novo peaks of chromatin accessibility unique to Clec16a-deficient β cells with >3,500 peaks that were absent when compared to control β cells (Figure 5B). These changes included the loss of chromatin accessibility within the *Ins2* locus with de novo accessibility found within the *Atf3* locus in Clec16a-deficient β cells (Figures 5C-D).

GREAT predictions in Clec16a-deficient β cells revealed loss of peaks at regions related to the regulation of mitophagy, lysosomal transport, and glucose metabolic processes, consistent with known functions for Clec16a were evident in control β cells ([55,56]; Figure S7C). Further, GREAT predictions of de novo accessible chromatin regions in Clec16a-deficient β cells displayed changes in cellular responses to carbohydrate stimulus, abnormal pancreas development, and abnormal pancreatic β cell differentiation (Figure S7D). Importantly, we observed significant enrichment of transcription factor binding site motifs for key ISR transcription factors in Clec16a-deficient β cells by HOMER [57], with bZIP factors, including Atf4, Atf3, and Chop, the most enriched in β-Clec16a^{KO} animals (Figures 5G-H). Moreover, we observed loss of binding sites for several transcription factors important for β cell identity, maturity, and function in Clec16a-deficient β cells, including CTCF, Sp1, and NeuroD1 (Figures 5G-H; [58-60]). Taken together, these results suggest that mitochondrial retrograde signals lead to substantial modification of chromatin accessibility favoring transcriptional activation of the ISR and loss of cell identity and maturity.

Loss of mitochondrial function induces immaturity and the ISR in hepatocytes and brown adipocytes

Given the critical importance of mitochondrial health in metabolic tissues, we next asked if defects in mitochondrial quality control would induce comparable impairments in cell maturity in other metabolic tissues beyond β cells. To this end, we generated mice bearing liver-specific deletion of Mfn1/2 or Tfam, following intraperitoneal administration of adeno-associated virus 8 expressing Cre-recombinase under control of the hepatocyte-specific Tbg promoter (AAV8-Tbg^{cre}) to 12-week-old HFD-fed control mice, and Mfn1/2 or Tfam floxed animals (hereafter known as L-Mfn1/2^{DKO} or L-Tfam^{KO} mice, respectively; Figures 6A-C). In both models, we observed expected decreases in mtDNA content and alterations of expression of key OXPHOS subunits, including loss of mitochondrial-encoded mt-Co1 without overt reductions in mitochondrial mass, as measured by Tom20 levels (Figures 6D-I). We next observed physiologic and metabolic

defects in hepatocytes of Mfn1/2 and Tfam-deficient mice. L-Mfn1/2^{DKO} animals developed alterations in glucose tolerance and insulin sensitivity consistent with reduced hepatic glucose output, while L-Tfam^{KO} mice developed slight alterations in insulin sensitivity with notable hepatic lipid accumulation (Figures S8A-D). Signs of liver injury and dysfunction were also evident following loss of mitochondrial quality control, with significant decreases in serum cholesterol in L-Mfn1/2^{DKO} mice and increases in serum ALT and LDH in L-Tfam^{KO} mice (Figures 6J-L).

We next used RNAseq to begin to determine if loss of mitochondrial quality control promoted a common signature of activation of the mitochondrial ISR, induction of cell immaturity, and loss of terminal cell identity markers in hepatocytes. Similar to our observations in β cells, we observed that L-Mfn1/2^{DKO} or L-Tfam^{KO} mice also had significantly increased expression of canonical ISR targets without upregulation of *Bip* expression (Figure 6M). To determine if defects in mitochondrial quality control altered hepatocyte maturity, we overlaid RNAseq data on a curated list of key hepatocyte terminal identity and developmental markers [61]. We found decreased expression of terminal hepatocyte markers including genes associated with cytochrome P450 activity and bilirubin glucuronidation and increases in several markers of hepatocyte immaturity, including alpha fetoprotein (*Afp*), *Psat1*, and *Top2a* ([61]; Figures 6N-O). Moreover, we confirmed induction of the ISR by detection of increased phosphorylation of Eif2α and Atf4 protein levels, while also confirming expression of markers of hepatocyte immaturity by WB in both L-Mfn1/2^{DKO} and L-Tfam^{KO} mice (Figures 6P-S).

As mitochondrial health is well known to be crucial for brown adipocyte tissue (BAT) function, we next surveyed expression of terminal identity markers and the ISR from mice bearing adipocyte-specific deletion of cardiolipin synthase (Crls1), an enzyme essential for biosynthesis of the key mitochondrial phospholipid cardiolipin [62]. Notably, cardiolipin plays several crucial roles in mitochondrial health, including regulation of mitochondrial quality control through cardiolipin-dependent mitophagy [63,64]. To this end, we analyzed publicly available RNAseq data from BAT depots isolated from mice bearing adipocyte-specific deletion of *Crls1* generated by intercrossing

of *Crls1* floxed animals to the adiponectin Cre-recombinase strain (hereafter known as AdCKO mice; [62]). Notably, AdCKO mice were previously shown to develop reduced mitochondrial function, glucose uptake, and thermogenesis in BAT depots, however, a link between between cardiolipin metabolism and BAT maturity was not assessed [62]. We re-analyzed RNAseq data from AdCKO and control BAT depots, overlaying expression data on the BATLAS database, which includes numerous key terminal BAT identity/maturity markers [65]. Interestingly, we found a striking downregulation of numerous BATLAS genes, including a loss of BAT-specific genes associated with cellular maturity/identity, such as *Pgc1α* and *Ucp1* (Figure 6T). Further, we observed an induction of canonical ISR transcriptional targets in AdCKO BAT depots (Figure 6T). Taken altogether, these results highlight the vital role for mitochondrial health to promote terminal cell identity by restraining mitochondrial retrograde signaling in numerous metabolic tissues.

Elevations in mtROS or glucotoxic metabolic overload do not appear to contribute to β cell defects following mitophagy deficiency

We next endeavored to understand the potential upstream signals contributing to the loss of β-cell mass or function following disruption of mitochondrial quality control. Impaired mitochondrial metabolic output and excess mtROS have both been suggested to act as retrograde signals to activate the ISR and promote mitochondrial-nuclear crosstalk [51]. Further, chronic hyperglycemia has been suggested to induce loss of β-cell mass and maturity, which could potentiate excess generation of mtROS due to metabolic overload [23,66]. Thus, we used genetic and pharmacologic approaches to determine if excess mtROS or profound hyperglycemia contributes to the loss of β-cell mass or function in mitophagy-deficient mice.

To determine if enhanced mtROS contributes to loss of β-cell health, we intercrossed mice bearing the Cre recombinase-inducible mitochondrial-targeted human catalase (mCAT) inserted in the ubiquitously active GAPDH locus with β-*Clec16a*^{KO} mice or *Ins1*-Cre controls, to scavenge mtROS specifically in β-cells *in vivo* following Cre-mediated recombination without concerns for

systemic effects of pharmacologic antioxidants [67]. While mCAT primarily disposes of H_2O_2, β-cell-specific mCAT overexpression also has been shown to protect against other mitochondria-derived oxidants, including superoxide [68]. Following confirmation of overexpression of human catalase in isolated islets of β-*Clec16a*^{KO}; mCAT mice and *Ins1*-Cre; mCAT controls (Figure S9A), we assessed glucose tolerance, insulin sensitivity, and insulin secretion following diet-induced obesity. We again confirmed impairments of glucose tolerance and glucose-stimulated insulin secretion in HFD-fed β-*Clec16a*^{KO} mice without impaired insulin sensitivity compared to HFD-fed Ins1-Cre controls (Figures S9B-D). Notably, overexpression of mCAT did not ameliorate glucose intolerance or loss of insulin secretion in β-*Clec16a*^{KO}; mCAT mice, suggesting that mtROS is unlikely to be a primary driver of reduced β-cell mass or function following mitophagy-deficiency.

To next determine if glucotoxic metabolic overload contributes to loss of β-cell mass following impaired mitochondrial quality control, we administered the SGLT1/2 inhibitor phlorizin to HFD-fed β-*Clec16a*^{KO} and control animals to improve glycemic control via increased urinary glucose excretion. As we speculated that chronic hyperglycemia might be necessary to precipitate the loss of β-cell mass, we administered phlorizin by implantable mini-osmotic pumps for 6 weeks prior to physiologic and morphometric assays. We first confirmed that continuous phlorizin infusion substantially increased glycosuria both in HFD-fed control and β-*Clec16a*^{KO} mice (Figure S9E). Importantly, phlorizin treatment improved glucose tolerance in HFD-fed β-Clec16a^{KO} mice similar to the range of what we previously observed with RFD-fed β-*Clec16a*^{KO} animals, which do not develop reductions in β-cell mass (Figures 1F, 1I, and S9F). Despite the improvement in glycemic control, phlorizin treatment did not rescue impairments in glucose-stimulated insulin secretion or β-cell mass in HFD-fed β-Clec16a^{KO} mice. (Figures S9G-H). No differences in insulin sensitivity were observed between the groups (Figure S9I). Thus, these studies suggest that reduced β-cell mass, which is driven by loss of β-cell identity in mitophagy-deficient animals, does not appear to be a consequence of glucotoxic metabolic overload.

We next measured cellular ATP/ADP ratios as an indicator of metabolic output in β-cell models of impaired mitochondrial quality control. As mitochondria are well known to increase ATP levels following glucose stimulation, we measured ATP/ADP ratio following glucose stimulation as well as total ATP/ADP output following exposure to NaN_3 to quench all mitochondrial function. Notably, RFD-fed β-Clec16a^{KO} islets displayed a reduction of glucose-stimulated ATP/ADP ratios, which was further impaired in HFD-fed mitophagy deficient mice (Figure S9J). We next examined Tfam-deficient islets and noted substantial reductions in both glucose-stimulated as well as total ATP/ADP ratios following NaN_3 exposure (Figures S9L-M). These results suggest defects in metabolic outputs in both Clec16a and Tfam-deficient mice. Interestingly, the more substantial decline in metabolic function we observed following Tfam-deficiency correlates with the higher rates of insulin negative tdTomato positive immature β-cells observed when compared to β-Clec16a^{KO} animals. Taken altogether, these studies suggest that impaired mitochondrial metabolic output, rather than enhanced mtROS or glucotoxic overload, may act as an upstream contributor to loss of β-cell mass following mitochondrial dysfunction.

Blockade of retrograde signaling restores β-cell mass and maturity *in vivo*

Our results in numerous metabolic tissues implicate that mitochondrial dysfunction engages the ISR and induces loss of terminal cell maturity/identity. We therefore hypothesized that induction of retrograde mitochondrial signaling through the ISR directly leads to loss of cellular maturity. To test the importance of the ISR in β-cell maturity, we treated HFD-fed β-Clec16a^{KO} mice with ISRIB, a well described inhibitor of the ISR [69]. We first treated isolated islets from HFD-fed β-Clec16a^{KO} mice and controls with ISRIB for 24 hours, observing the expected reduction in Eif2α phosphorylation in both groups following ISRIB exposure (Figure 7A). Concordantly, we found that inhibition of the ISR was able to abrogate the induction of ISR transcriptional targets, including *Cebpβ* and *Trib3*, in islets from HFD-fed β-Clec16a^{KO} mice (Figures 7B-C). Importantly, we also found that ISRIB reduced expression of the dedifferentiation

marker Aldh1a3 and restored the terminal β-cell identity marker *Ucn3* in islets from HFD-fed β-Clec16a^{KO} mice (Figures 7A, 7D). To determine if the restoration of β-cell identity was possibly due to an unanticipated upregulation of mitophagy in Clec16a-deficient β-cells, we intercrossed β-Clec16a^{KO} mice with the mt-Keima mitophagy reporter strain to assess mitophagy flux (Figure 7E). Importantly, islets of ISRIB-treated β-Clec16a^{KO} mice continued to maintain the well-known defects in mitophagy flux expected following Clec16a-deficiency (Figure 7E), suggesting the restoration of β-cell identity markers by ISRIB was not due to enhanced mitophagy but rather related to blockade of retrograde signaling through the ISR.

To next determine if retrograde signaling through the ISR leads to loss of β-cell mass and identity *in vivo*, we treated HFD-fed β-Clec16a^{KO} mice and littermate controls with ISRIB by daily intraperitoneal administration for 4 weeks (Figure 7F). Notably, extended treatments with ISRIB in control animals *in vivo* did not impair β-cell mass, glucose tolerance, or insulin sensitivity, consistent with a previous report (Figures 7G-J) [70]. Strikingly, ISRIB was able to rescue the loss of β-cell mass in HFD-fed β-Clec16a^{KO} mice (Figure 7G). We also observed that ISRIB ameliorated glucose intolerance in HFD-fed β-Clec16a^{KO} mice, while peripheral insulin sensitivity was unchanged between groups (Figure 7H-J). Importantly, ISRIB treatment reduced expression of Aldh1a3 in HFD-fed β-Clec16a^{KO} mice as well as increasing the frequency of Ucn3 positive β cells bearing proper expression/localization of Glut2, consistent with restoration in β cell maturity and identity (Figures 7K-P). Thus, blockade of the ISR can restore β cell mass, function, and maturity following mitochondrial dysfunction. Taken altogether, these studies position the induction of mitochondrial retrograde signaling through the ISR as a direct regulator of cell maturity and identity in metabolic tissues.

DISCUSSION

Mitochondria are pivotal cellular organelles, which provide the energy required for cellular function, growth, division, and survival. Here, we demonstrate that mitochondrial dysfunction

engages a retrograde signaling response shared across metabolic tissues, which ultimately impairs cellular identity and maturity. Perturbations at any point within the mitochondrial quality control machinery converge to activate the ISR, eliciting a transcriptional signature associated with an induction of cellular immaturity and modulation of chromatin architecture. We also clarify the metabolic signals which activate the ISR upon mitochondrial dysfunction. Intriguingly, changes in terminal cell identity are reversible as inhibition of the mitochondrial ISR restores cellular maturity, mass, and function. Together, we demonstrate that mitochondrial function plays a central role in the control of cell identity in metabolic tissues.

Our studies implicate a crucial role for retrograde mitochondrial control of cellular identity and maturity. While the functions of classical anterograde (nuclear to mitochondrial) control of metabolism are well known, retrograde signals generated from the mitochondria have less clear roles in the regulation of mammalian cellular homeostasis [51,71,72]. Transcriptional regulators of BAT and β cell maturity and identity, including Prdm16, Pgc1α, Pdx1, Foxo1, and ERRγ, have been associated with anterograde control of mitochondrial metabolism [35,73-77], yet it has not been established that mitochondrial resident proteins directly feedback to the nucleus to control cell maturity and identity. Retrograde signaling in yeast through the transcriptional regulators Rtg1, 2 and 3 have been well characterized [78-80], yet mammalian orthologs of these factors have proved elusive to date. Interestingly, the Rtg family has been implicated in the modulation of TCA cycle enzymes, glutamate biosynthesis and mtDNA maintenance but not in cellular identity [80]. Whereas mammalian Rtg gene orthologs have yet to be discovered, distinct retrograde signaling pathways are present in mammalian cells, including the mitochondrial unfolded protein response (UPR^{mt}) and the integrated stress response (ISR). Activation of both the ISR and UPR^{mt} have been previously implicated in the regulation of cell survival, yet the control of cellular identity or maturity have not been described [51]. Thus, our studies position a new role for retrograde signaling following mitochondrial dysfunction to impair cellular maturity, ultimately leading to the deterioration of metabolic tissues.

We observe substantial changes in chromatin accessibility following the induction of mitochondrial dysfunction and activation of the ISR. The increased frequency of binding motifs related to the central ISR transcriptional regulator ATF4 as well as ATF4 targets is suggestive that retrograde signaling may also alter chromatin structure. Indeed, previous studies have positioned ATF4 as a pioneer factor capable of altering chromatin accessibility [81], which could be consistent with the transcriptional signatures observed in metabolic tissues with mitochondrial damage. However, it is unclear how the induction of ATF4 remodels sites of chromatin accessibility that are lost pertaining to key markers of β cell maturity, such as NeuroD1. Loss of binding regions essential for β cell maturity following mitochondrial dysfunction could also lead to impaired substrate availability and metabolism eventually affecting epigenetic modifications, similar to metabolic control of epigenetics reported in the cancer biology literature [82]. Thus, we speculate that defects in bioenergetic capacity following mitochondrial dysfunction could have a cascade of effects to reprogram metabolic tissues, initiated by activation of the ISR to remodel chromatin architecture and support cellular alterations to an immature state. Exploration of the metabolic control of chromatin accessibility following mitochondrial dysfunction, and how these effects may be tuned upstream by both substrate metabolism and metabolic sensors of the ISR, including the kinases PERK, GCN2, HRI, and PKR [83], will be intriguing candidates for future study.

Mitochondrial health is central to the function of metabolic tissues, yet frequently viewed as a client organelle tasked with energy generation or apoptotic signaling rather than as a primary driver of cell fate. Indeed, the appearance of mitochondrial dysfunction in metabolic tissues during diabetes or other metabolic diseases is often considered an indirect consequence of other etiologies, including transcriptional defects, ER stress, or nutritional excess [84-86]. We observe key defects across the spectrum of the mitochondrial quality control pathway in human β-cells during T2D that are sufficient to elicit β-cell immaturity in isolation in genetic mouse models or primary human islets. The remarkable consistency of these connections between mitochondrial dysfunction and cellular immaturity across human and rodent metabolic tissues further supports

the central importance of mitochondria to maintain terminal cell identity, which to our knowledge has not previously been described. Moreover, our findings reinforce the importance of signatures of mitochondrial dysfunction in human β-cells of pre-diabetic donors with impaired glucose tolerance, potentially implicating that mitochondrial dysfunction preceding T2D is an etiopathological defect in β-cells that possibly extends to other tissues. It will be intriguing to determine if preemptively targeting mitochondrial health or retrograde signaling could prevent the onset of metabolic diseases.

RESOURCE AVAILABILITY

Lead Contact

Further information and request for resources and reagents should be directed to and will be fulfilled by the lead contact, Scott Soleimanpour (ssol@med.umich.edu)

Materials Availability

Rabbit polyclonal Clec16a antisera, available on request from the lead author. mtKeima mice were maintained on the C57BL/6N background and eventually intercrossed to Clec16a$^{f/f}$ mice to generate mtKeima-Ctrl and mtKeima-β-Clec16a^{KO} mice; these mice are available on request from the lead author.

Data Availability

Bulk RNA-seq, single nuclei RNA-seq and single nuclei ATAC-seq data have been deposited at GEO and are publicly available as of the date of publication. Accession numbers are listed in the key resources table. This paper also analyzed existing publicly available data and the accession numbers for the datasets are listed in the key resources table. Original, uncropped western blot images have been deposited at Mendeley and are publicly available as of the date of publication. The DOI is listed in the key resources table. Microscopy data will be shared by lead contact on request.

Any additional information required to reanalyze the data reported in this paper is available from the lead author on request.

EXPERIMENTAL MODEL AND SUBJECT DETAILS

Genetically modified mouse lines*:* All mice were maintained in accordance with the University of Michigan's Institutional Animal Care and Use Committee under specific pathogen free conditions. Up to 5 mice were housed per cage and were maintained on regular chow or high fat diet chow *ad libitum* on a 12 h light-dark cycle. Floxed Tfam (Tfam$^{f/f}$ mice (Jackson Laboratories, Stock no. 026123)), Clec16a (Clec16a$^{f/f}$ mice [55]), Mfn1/2 (Mfn1$^{f/f}$/Mfn2$^{f/f}$ mice (Jackson Laboratories stock no. 026401 and 026525), Rosa26 lox-STOP-lox tdTomato reporter mice (Jackson Laboratories, Stock no. 007914), and floxed stop mCAT overexpression mice (Jackson Laboratories, Stock no. 030712) were used. To generate β-cell specific deletion, floxed models were crossed with Ins1-Cre mice from Jackson laboratories (JAX Stock No. 026801). For inducible β-cell deletion, MIP1-CreERT mice (JAX 024709) were used or crossed to Clec16a$^{f/f}$ mice to generate iβ-Clec16a^{KO} mice as previously described [56]. To induce knockout in this model, 7 wk old mice were injected intraperitoneally with 2mg of tamoxifen (Cayman Chemicals) in corn oil every other day for 3 days. *Ins1*-Cre–alone and respective floxed only controls for each study (Tfam$^{f/f}$, Mfn1$^{f/f}$/Mfn2$^{f/f}$, or Clec16a$^{f/f}$ mice) were phenotypically indistinguishable from each other and combined as controls (Ctrl) as noted, with the exception of lineage tracing studies where controls were *Ins1*-Cre only. *Ins1*-Cre–alone were also phenotypically indistinguishable from wild-type C57BL/6N controls, consistent with previous reports from our group and others [31,32,37,87]. For liver specific deletion, tdTomato reporter, Tfam$^{f/f}$, and Mfn1$^{f/f}$/Mfn2$^{f/f}$ mice at 16 wk of age were injected intraperitoneally with $2x10^{11}$ particles of AAV-Tbg^{cre} (AAV8 serotype; Vector Biolabs; San Francisco, CA, USA) and placed on high fat diet for 6 wk. Mixed sex cohorts were used throughout. Male only mice were used for ISRIB *in vivo* dosing experiments due to the short duration of diet, and necessity for the largest diet-induced effect during this time period. Mice were between 7 weeks and 1 year of age at the time of study, depending on endpoint (information is

provided in the text). Mice were randomized into treatment or vehicle control groups and/or regular chow or high fat diet groups, as necessary.

Human islet samples: All human samples were procured from de-identified donors with or without diabetes from the Integrated Islet Distribution Program and approved by the University of Michigan Institutional Review Board. Human primary islets were cultured at 37°C with 5% CO_2 in PIM(S) media (Prodo Laboratories, Aliso Viejo, CA, USA) supplemented with 10% FBS, 100U/ml penicillin/streptomycin, 100U/ml antibiotic/antimycotic, and 1mM PIM(G) (Prodo Laboratories, Aliso Viejo, CA, USA). Islets were used from male and female donors.

Mouse primary islet cultures: Mouse primary islets were isolated by perfusing pancreata with a 1mg/ml solution of Collagenase P (Millipore Sigma; St Louis, MO, USA) in 1 X HBSS into the pancreatic duct. Following excision of the pancreas, pancreata were incubated at 37°C for 13 min, and Collagenase P was deactivated by addition of 1XHBSS + 10% adult bovine serum (Quench buffer). Pancreata were dissociated mechanically by vigorous shaking for 30 sec, the resulting cell suspension was passed through a 70μM cell strainer (Fisher Scientific, Waltham, MA, USA). Cells were centrifuged at 1000rpm for 2 min, the pellet was resuspended in 20 ml Quench buffer and gently vortexed to thoroughly mix. Cells were again centrifuged at 1000 rpm, 1 min. This wash step was repeated once more. Following washes, the cell pellet was resuspended in 5ml Histopaque (Millipore-Sigma; St Louis, MO, USA) with gentle vortexing. An additional 5 ml Histopaque was layered on the cell suspension, and finally 10ml Quench buffer was gently layered on top. The cells were spun at 900 x g for 30 min at 10°C, with the brake off. The entire Histopaque gradient was pipetted off and passed through an inverted 70μM filter, to trap the islets cells. Islets were washed twice with 10 ml Quench buffer and once with complete islet media (RPMI-1640 supplemented with 100U/ml penicillin/streptomycin, 10% FBS, 1mM HEPES, 2mM L-Glutamine, 100U/ml antibiotic/antimycotic and 10mM sodium pyruvate). The filter was inverted

into a sterile petri dish and cells were washed into the dish with 4.5ml complete islet media. Islets were left to recover overnight, and treatments began the next day. Mouse islets were treated with ISRIB (100nM, 24 h), Valinomycin (250μM, 3 h), or vehicle controls, and were isolated from both male and female mice.

METHOD DETAILS

High Fat feeding: Ins1-Cre or β-Clec16a^{KO} mice were randomized into 10% regular fat diet or 60% high fat diet (Research Diets Inc; New Brunswick, NJ, USA) at weaning. Access to food was *ad libitum* for 12 weeks. Mice were then subjected to *in vivo* metabolic analyses as required (detailed in following sections), and pancreatic tissue was harvested at the end of the study for immunohistochemistry, *ex vivo* islet studies or RNA-Seq analysis.

Intraperitoneal Glucose Tolerance Tests (IPGTT): Mice were fasted for 6 h. Fasting blood glucose measurements were taken by tail nick (Bayer Contour glucose meter) before an IP injection of 2mg/kg glucose was administered. Blood glucose measurements were then taken at 15, 30, 60 and 120mins. Following the test mice were returned to housing cages with *ad libitum* to food.

***In vivo* Glucose Stimulation Insulin Secretion (GSIS) test:** Mice were fasted to 6 h. Fasting blood glucose was measured after tail nick with a glucometer (Bayer Contour) and a 20μl blood sample was collected using capillary tubes (Fisher Scientific) and stored on ice. Mice were injected with 3mg/kg glucose and blood glucose and blood samples were taken after 3min. Blood samples were ejected from the capillary tubes into 1.5ml tubes, spun at 16,000 x *g*, 4°C for 10min, and serum was aliquoted to new 1.5ml tubes. Serum insulin levels were measured by insulin ELISA (Alpco; Salem, NH). Following the test mice were returned to housing cages with *ad libitum* to food.

Intraperitoneal Insulin Tolerance Tests (ITT): Mice were fasted for 6 h. Fasting blood glucose was measured after tail nick with a glucometer (Bayer Contour). Mice were injected with 1U/kg (males) or 0.75U/kg (females) insulin (Humulin R; Eli Lilly; Indianapolis, IN) and blood glucose measured at 15, 30, and 60min. Glucose (20% w/v solution) was administered if mice became hypoglycemic (blood glucose below 25mg/dl). Following the test mice were returned to housing cages with *ad libitum* to food.

Mini-osmotic pump implantation: Clec16a$^{f/f}$ or β-Clec16a^{KO} mice were fed high fat diet for 6 weeks before osmotic pump implantation. While under isoflurane anesthesia all mice were implanted subcutaneously with an Alzet micro-osmotic pump (model 2006, Durect, Cupertino, CA, USA) with either vehicle or phlorizin (0.8 mg/kg/d for 6 weeks) as previously described [88]. Mice were monitored for wound healing and treated with topical pain relief and antibiotics as required. Mice continued on high fat diet for another 6 weeks, with weekly weight and urine glucose measurement by Diastix (Bayer; Whippany, NJ, USA). ITTs were carried out in week 11, and IPGTT and *in vivo* GSIS in week 12, followed by pancreas harvest.

***In vivo* ISRIB treatment:** Male Clec16a$^{f/f}$ or β-Clec16a^{KO} mice were placed on high fat diet at weaning, one week later they were randomized into Vehicle (40% saline;50% polyethylene glycol; 10% DMSO) or 2.5μg/g/day ISRIB delivered intraperitoneally daily for 5 weeks. ITTs were carried out at the beginning of week 4, IPGTTs at the end of week 4, and followed by pancreas harvest.

Mitophagy assessment in live mouse islets using mtKeima: mtKeima-Ctrl or mtKeima-β-Clec16a^{KO} islets were isolated and treated for 24 h with vehicle (DMSO) or 100nM ISRIB. On the day of analysis, islets were treated with ctrl (DMSO) or 250μM Valinomycin for 3 h. Islets were dispersed to single cells using 500μl 0.25% trypsin and incubation at 37C for 3min followed by

gentle pipetting and neutralization of the trypsin with FACS buffer (RPMI1640 phenol free + 1% BSA). Single cells were sedimented by centrifugation at room temperature, 2000 rpm, 1 min, and the pelleted cells were washed twice with 1X PBS. The cells were resuspended in 500µl FACS buffer, transferred to FACS tubes, and incubated with 500nM Fluozin-3 for 30 min at 37°C, to label Zn^{2+} enriched insulin granules in β-cells. Cells were centrifuged at 1400rpm for 3min and resuspended in 500µl FACS buffer. Samples were analyzed on an LSR Fortessa flow cytometer (BD Biosciences). Single cells were gated using forward scatter and side scatter (FSC and SSC, respectively) plots, DAPI staining was used to exclude dead cells, and Fluozin-3 was used to identify β cells. Mitophagy measurements were made using dual laser excitation at 407nm and 532nm with an emission laser of 605 nm, as previously described [33], and results were analyzed with FlowJo (Tree Star Inc). A total of 5,000 β cells were analyzed per individual experimental replicate.

Mitophagy assessment in live human islets: Human islets from non-diabetic or Type 2 Diabetic (T2D) donors were cultured for a maximum of 48 h after shipment. On the day of the experiment islets were incubated with 100nM MTphagy dye (Dojindo Molecular Technologies; Rockville, MD, USA) for 30 min. Vehicle (DMSO) or 1mM Valinomycin was then added to the islets for 3 h. Islets were then dispersed to single cells using 500µl 0.25% trypsin and incubation at 37C for 3min. This was followed by gentle pipetting up and down approx. 10 times and neutralization of the trypsin with human islet FACS buffer (1X KRBH + 1% BSA). Single cells were sedimented by centrifugation at room temperature, 2000 rpm, 1 min, and the pelleted cells were washed twice with 1X PBS. The cells were resuspended in 500µl human islet FACS buffer, transferred to FACS tubes, and incubated with 500nM Fluozin-3 and 2.5nM TMRE for 30 min at 37°C to label insulin granule positive β cells and mitochondrial membrane potential respectively. Cells were centrifuged at 1400rpm, room temperature, 3min and resuspended in 500µl human islet FACS buffer. Samples were analyzed on an LSR Fortessa flow cytometer (BD Biosciences). Single cells

were gated using forward scatter and side scatter (FSC and SSC, respectively) plots, DAPI staining was used to exclude dead cells, and Fluozin-3 was used to identify β-cells. Mtphagy measurements in β-cells were made using 488 nm excitation laser with a 710 nm emission filter and analyzed using FlowJo (Tree Star Inc.). A total of 5,000 β cells was quantified from each independent islet preparation.

mtDNA assessment in human islets: 25 human islets per donor were hand picked and washed 2 X with 1X PBS. Islets were pelleted and stored at -80°C until DNA extraction using the Blood/Tissue DNeasy kit (Qiagen; Germantown, MD, USA) as per manufacturer's instructions. Relative mtDNA content was quantified by qPCR using mtDNA specific primers ND1, and nuclear DNA specific primers for B2M as previously described [89].

mtDNA assessment in flow sorted mouse islets: Mouse islets were isolated from 4 individual Ins1-Cre or β-Tfam^{KO} mice and left to recover overnight. The following day, islets were dispersed to single cells (as per mt-Keima FACS protocol) and sorted on a FACSAria III cell sorted (BD Biosciences). Single cells were gated using forward scatter and side scatter (FSC and SSC, respectively) plots, DAPI staining was used to exclude dead cells, and β cells were sorted from non-β cells based on high 561nm excitation, 582nm emission. Positive and negative cell populations were collected in 1X PBS from each mouse, spun to pellet and DNA was extracted using the Blood/Tissue DNeasy kit (Qiagen). Relative mtDNA content was quantified by qPCR using mtDNA specific primers Mt9 and Mt11, and nuclear DNA specific primers Ndufv1 Forward and Reverse [90].

β-cell mass analysis: Whole mouse pancreas was excised, weighed, and fixed in 4% paraformaldehyde for 16 h at 4°C. Samples were stored in 70% ethanol, 4°C before being embedded in paraffin and sectioned. 3 independent depths of sections, at least 50μM away, were

dewaxed, and rehydrated and antigen retrieval was carried out using 10mM sodium citrate (pH 6.0) in a microwave on high for 10min. Sections were washed 2X with 1X PBS, blocked for 1 h at room temperature with 5% donkey serum in PBT (1X PBS, 0.1% Triton X-100, 1% BSA). Sections were then incubated in the following primary antisera overnight at 4°C in PBT: guinea pig anti-insulin (Abcam; Waltham, MA, USA), rabbit anti-glucagon (Santa Cruz; Dallas, TX, USA). Sections were then washed 2 X with PBS and incubated for 2 h at room temperature with species specific Cy2 and Cy3 conjugated secondary antibodies. Nuclear labelling was performed using DAPI (Molecular Probes). Sections were scanned using an Olympus IX81 microscope (Olympus; Center Valley, PA, USA) at 10X magnification, with image stitching for quantification (Olympus). β-cell mass quantification (estimated as total insulin positive area/total pancreatic area multiplied by pancreatic weight) was performed on stitched images of complete pancreatic sections from 3 independent depths.

Immunofluorescence of paraffin embedded sections: Whole mouse pancreas was excised, weighed, and fixed in 4% paraformaldehyde for 16 h at 4°C. Samples were stored in 70% ethanol at 4°C, before being embedded in paraffin and sectioned. For Aldh1a3/Pdx1 staining, antigen retrieval was carried out using 1 X HistoVT buffer (Nacalai USA Inc; San Diego, CA, USA) in an antigen retriever pressure cooker (Electron Microscopy Sciences; Hatfield, PA, USA). Sections were washed 2 X with 1X PBS, blocked for 1 h at room temperature with 1 X Blocking One solution (Nacalai USA Inc; San Diego, CA, USA). Sections were then incubated in the following primary antisera overnight at 4°C in 1 X PBS + 1% tween + 20% Blocking One solution: rabbit anti-Aldh1a3 (Novus Biologicals; Littleton, CO, USA). Sections were then washed 2 X with PBS and incubated for 2 h at room temperature with species specific Cy2 and Cy3 conjugated secondary antibodies. For Ucn3/Pdx1 staining, antigen retrieval was carried out using 10mM sodium citrate (pH 6.0) in a microwave on high for 10min. For Glut2/Pdx1 staining, antigen retrieval was carried out using 1 X R-Buffer A (Electron Microscopy Sciences; Hatfield, PA, USA) in an antigen retriever pressure

cooker (Electron Microscopy Sciences; Hatfield, PA, USA). Sections were then washed 2 X with 1X PBS, blocked for 1 h at room temperature with 5% donkey serum in PBT. Sections were then incubated in the following antisera overnight at 4°C in PBT: rabbit anti-Ucn3 [91], or rabbit anti-Glut2 (Millipore Sigma; St Louis, MO, USA) and goat anti-Pdx1 (Abcam; Waltham, MA, USA). Sections were then washed 2 X with PBS and incubated for 2 h at room temperature with species specific Cy2 and Cy3 conjugated secondary antibodies. Nuclear labelling was performed using DAPI (Molecular Probes). Images were captured under 100X oil immersion magnification on an Olympus IX81 microscope. Quantification of co-positive cells was carried out by a blinded third party researcher, and samples were re-identified after quantification to reduce bias.

Lineage tracing immunofluorescence analysis: Whole pancreas was excised, weighed, and fixed in 4% paraformaldehyde for 16 h before being washed with 70 % ethanol and incubated with 50% sucrose solution in PBS overnight. Pancreata were then embedded in OCT (ThermoFisher; Waltham, MA, USA) and frozen and stored at -80°C. 10μM sections were cut using a Leica CM3050 Cryostat at -20°C, and the slides were stored at -80°C until imaging. Sections were thawed briefly, washed 2X with 1X PBS, blocked with 5% donkey serum in PBT, and incubated overnight at 4°C with the following primary antisera: guinea pig anti-insulin (Abcam; Waltham, MA, USA) and rabbit anti-glucagon (Santa Cruz; Dallas, TX, USA). Sections were then washed 2 X with PBS, and incubated for 2 h at room temperature with species specific Cy2 and Cy5 conjugated secondary antibodies, endogenous tdTomato was bright enough to capture without antibody detection. Nuclear labelling was performed using DAPI (Molecular Probes). Images were captured on a Nikon A1 Confocal microscope at 40X oil immersion magnification, z-stacks were captured to ensure quantification of single planes of cells. Quantification of tdTomato/Insulin- and tdTomato/Glucagon+ cells was carried out.

Pseudoislets: Pseudoislets were prepared using the protocol described by Walker et. al. [54]. Briefly, human islets were handpicked and then dispersed with trypsin (Thermo Scientific). Islet cells were counted and incubated with adenovirus expressing shRNA against human TFAM or a scramble control for 2hr at MOI of 500. Cells were then seeded at 2000 cells per well in CellCarrier Spheroid Ultra-low attachment microplates (PerkinElmer) in enriched Vanderbilt pseudoislet media. Cells were allowed to reaggregate for 7 days before being harvested for cryosections or RNA.

Immunoblot analysis: Isolated mouse islets, human pseudoislets or frozen liver tissue was homogenized in RIPA buffer containing protease and phosphatase inhibitors. Samples were centrifuged at full speed for 10min, 4°C to pellet insoluble material and the supernatant was used in protein immunoblot analysis. Protein quantification was carried out using a Pierce micro BCA kit (ThermoFisher; Waltham, MA, USA). Up to 25µg of protein for islets and pseudoislets, or 150µg of protein for liver was prepared in Laemmeli buffer and DTT and denatured at 70°C for 10min, or 37°C for 30min for oxphos cocktail analysis. Samples were then run on a 4-12% Bis-Tris protein gel (Bio-Rad; Hercules, CA, USA) at 150V until separated. Protein was then transferred to a nitrocellulose membrane at 90V for 90min, membranes were blocked with 5% skim milk in 1X TBS + 0.05% tween and incubated overnight at 4°C with primary antisera. Membranes were then washed 3X with 1X TBS+0.05% tween and incubated with species-specific HRP conjugated secondary antisera (Vector Labs).

Perceval imaging: The ATP/ADP ratio was monitored using the PercevalHR biosensor [92]. Islets were perifused with 16.7 mM glucose to stimulate ATP production in a recording chamber on an Olympus IX-73 inverted epifluorescence microscope (Olympus). PercevalHR was excited at 488 nm using a TILL Polychrome V monochromator (FEI), and a QuantEM:512SC cooled CCD

camera (PhotoMetrics) was used to collect emission at 527 nm [93]. Data were acquired and analyzed using Metafluor (Invitrogen) and plotted using Igor Pro (WaveMetrics Inc.).

Bulk RNA-Seq of liver: Sequencing was performed by the Advanced Genomics Core at University of Michigan Medical School. Total RNA was isolated from frozen liver samples and DNase treated using commercially available kits (Omega Biotek and Ambion, respectively). Libraries were constructed and subsequently subjected to 151bp paired-end cycles on the NovaSeq-6000 platform (Illumina). FastQC (v0.11.8) was used to ensure the quality of data. Reads were mapped to the reference genome GRCm38 (ENSEMBL), using STAR (v2.6.1b) and assigned count estimates to genes with RSEM (v1.3.1). Alignment options followed ENCODE standards for RNA-seq. FastQC was used in an additional post-alignment step to ensure that only high-quality data were used for expression quantitation and differential expression. Data were pre-filtered to remove genes with 0 counts in all samples. Differential gene expression analysis was performed using DESeq2, using a negative binomial generalized linear model (thresholds: linear fold change >1.5 or <-1.5, Benjamini-Hochberg FDR (P_{adj}) <0.05). Plots were generated using variations of DESeq2 plotting functions and other packages with Genialis (Boston, MA, USA).

Nuclear isolation from mouse islets: Isolated islets were handpicked, washed 2X with PBS, and dissociated to single cells with 500µl 0.25% trypsin at 37°C for 3min followed by vigorous pipetting and quenching with complete islet media. Single cells were washed 2X with PBS and finally resuspended in 1X HBSS + 200U/ml DNAse and incubated at 37°C for 30min. Cells were washed 4X with PBS to ensure removal of DNAse and resuspended in PBS + 1% BSA. Viability was checked using trypan blue, and only samples above 80% viability were carried forward. Cells were split evenly into 2 portions for differential snRNA and snATAC isolation protocols. For snRNA: Cells were pelleted at 500 x g for 5min, 4°C, and lysed with 50µl RNA-LB (10mM Tris-

HCl pH7.4, 10mM NaCl, 3mM $MgCl_2$, and 1% NP-40 in sterile nuclease free water) by incubation on ice for 3min. Nuclei were pelleted at 500 x g for 5min, 4°C, washed in 500µl wash buffer (1X PBS, 1% BSA and 0.2U/µl RNAse inhibitor), spun at 500 x g for 5 min, 4°C and finally responded in 100µl wash buffer. For snATAC: Cells were pelleted at 500 x g for 5 min, 4°C and lysed in 50µl ATAC-LB (10mM Tris-HCl pH7.4, 10mM NaCl, 3mM $MgCl_2$, 0.1% NP-40, 0.1% tween20 and 0.01% digitonin in sterile nuclease free water) by gentle pipetting 5X and incubation on ice for 3min. 1mL ATAC-wash buffer (10mM Tris-HCl pH7.4, 10mM NaCl, 3mM $MgCl_2$ and 0.1% tween20 in sterile nuclease free water) was added and samples spun at 500 x g for 5min, 4°C. Nuclei were resuspended in nuclei buffer (10X Genomics). After all nuclei isolation protocols, nuclei were counted and the Advanced Genomics Core at the University of Michigan processed the samples for sequencing.

Single nucleus RNA sequencing (snRNA-seq) and quantification: Approximately 14,000 single nuclei were loaded onto a 10X Genomics Chromium machine and resulting captured cells were sequenced via 10X Genomics Single Cell 3P v3 chemistry (10x Genomics, USA), yielding approximately 7k nuclei per lane. All libraries were analyzed using the Cell Ranger analysis pipeline version 3.0. Briefly, reads were aligned to mouse reference sequence mm10 and unique molecular identifiers (UMIs) were quantified using the Cell Ranger “count” software with default parameters. Count data from each single nucleus were normalized to the same sequencing depth and then aggregated using the “cellranger aggr” tool. Cell barcodes with fewer than 1000 detected genes and a total mitochondrial content >20% (signifying potential apoptotic cells) were discarded from analyses.

Single nucleus ATAC sequencing (snATAC-seq) and quantification: Approximately 14,000 single nuclei were loaded and sequenced via 10X Genomics Single Cell ATAC v1 chemistry (10x Genomics, USA), yielding approximately 7K cells per lane. All libraries were sequenced

individually on Illumina NovaSeq S4 flowcells and were analyzed using the Cell Ranger ATAC analysis pipeline version 1.2.0. Reads were similarly aligned to mouse reference sequence mm10 and fragments, open chromatin peaks were quantified using the Cell Ranger ATAC "count" software with default parameters. Fragment data from each single cell library were normalized to the same sequencing depth and then aggregated using the "cellranger aggr" tool. Resultant genomic alignment (BAM) files were filtered to contain only nucleosome free reads (<147 bp) using SAMtools version 1.8 [94].

snRNA-seq doublet cell detection and removal: To identify and remove potential multiplet droplets from snRNA-seq data, we used DoubletFinder [95] and Scrublet [96] to identify multiplet nuclei in an unbiased/non-cell type specific manner. For both methods, we assumed an expected doublet rate of 10% of total cells. Afterwards, we removed all multiplet nuclei identified by at least one of these two methods (union set of doublets).

snRNA-seq cell clustering: Nuclei were clustered using top 2000 most variable genes, which are determined by fitting a line to the relationship of the variance and mean using a local polynomial regression (loess). Gene expression values were standardized using the observed normalized mean and expected variance (given by the fitted line). Feature variance was then calculated on the standardized values after clipping to a maximum of the square root of the number of cells. After scaling and centering the feature values, principal component analysis (PCA) was performed on the top 2000 variable features. Following this, uniform manifold approximation and projection (UMAP) was applied on the top 20 principal components to reduce the data to two dimensions. Next, a shared nearest neighbor (SNN) graph was created by calculating the neighborhood (Jaccard index) overlap between each cell and its 20 (default) nearest neighbors. To identify cell clusters, we used a SNN modularity optimization-based clustering algorithm [97].

Annotation of cell types in snRNA-seq: Islet cell clusters were annotated based on expression of known cell-type markers —*Ins1/2* (beta), *Gcg* (alpha), *Sst* (delta). The remaining cells were annotated using pathway databases and annotations from the *clusterProfiler* (version 3.14.0 [98]) R package.

Differential gene expression analysis: Differential expression analyses was performed using the FindMarkers function (with default parameters) and the wilcox test option in the R package Seurat [97] to identify genes that are enriched in each cell type. In each comparison, protein coding genes and long intergenic non-coding RNAs (lincRNAs) with one or more UMIs in at least 10% of either cell type population being compared was used. Differentially expressed genes with FDR < 5% were regarded as significant results.

Pathway analysis of differentially expressed genes: Differentially expressed genes for each cell-type were functionally annotated using the R package *clusterProfiler* (version 3.14.0 [98]). The Kyoto Encyclopedia of Genes and Genomes (KEGG), gene ontology (GO), and WikiPathways databases were used to determine association with particular biological processes, diseases, and molecular functions. The top pathways with an FDR-adjusted p-value <5% were summarized in the results.

Integration of snRNA-seq and snATAC-seq data: Integrative clustering and analysis of single nuclei transcriptomes and single nucleus epigenomes was performed using the R package Seurat [97]. First, gene activity scores were derived from the resultant snATAC-seq peak count-matrix using the CreateGeneActivityMatrix function with default parameters. Next, single nuclei with < 5,000 total read counts were discarded from analyses. The resultant single nuclei and gene activity scores were log normalized and scaled. Using the processed snRNA-seq data (also analyzed

with Seurat), we identified anchors between the snATAC-seq gene activity score matrix and snRNA-seq gene expression matrix following the methodology described in [97]. After identifying anchors between the datasets, cell-type labels from the snRNA-seq dataset were transferred to the snATAC-seq dataset and a prediction and confidence score was assigned for each cell.

Aggregation of single nucleus ATAC-seq profiles into pseudo-bulk profiles: For each cell-type, single nucleus ATAC-seq profiles were aggregated into single bulk ATAC-seq profiles using using SAMtools version 1.8 [94] and the "merge" command. Merged BAM files were sorted and indexed using SAMtools and provided as input to identify open chromatin peaks. Peaks were called using MACS version 2.1.0.20151222 and the following parameters "-g 'mm' --nomodel --call-summits --qval 0.01 --keep-dup all -B -f BAMPE". Cell-type specific open chromatin peaks were identified using BEDtools version 2.27.0 [99] and the "bedtools intersect -v" command.

Transcription factor motif enrichment analysis: The *findMotifsGenome.pl* (HOMER version 4.6 [57]) script with parameters "hg19 -size 200" was used to determine TF motifs enriched in ATAC-seq peaks for KO beta cells relative to control beta cells (and vice versa). As an example, to identify TF motifs enriched in KO beta cell-specific peaks, we provided these peaks as the foreground, and the control beta cell-specific peaks as the background.

Statistics

In all figures, data are presented as means ± SEM, and error bars denote SEM, unless otherwise noted in the legends. Statistical comparisons were performed using unpaired two-tailed Student's t-tests, one-way or two-way ANOVA, followed by Tukey's or Sidak's post-hoc test for multiple comparisons, as appropriate (GraphPad Prism). A P value < 0.05 was considered significant.

Acknowledgements

S.A.S was supported by the JDRF (CDA-2016-189, COE-2019-861), the NIH (R01 DK108921, U01 DK127747), the Department of Veterans Affairs (I01 BX004444), the Brehm family, and the Anthony family. G.L.P. was supported by the American Diabetes Association (19-PDF-063). B.A.K. was supported by the Department of Veterans Affairs (I01 BX004444). The JDRF Career Development Award to S.A.S. is partly supported by the Danish Diabetes Academy and the Novo Nordisk Foundation. We acknowledge the Microscopy, Imaging and Cellular Physiology Core of the University of Michigan DRC (P30 DK020572) for assistance with imaging studies. We thank the University of Michigan Flow Cytometry Core for assistance with flow cytometry studies. Next generation sequencing was carried out in the Advanced Genomics Core at the University of Michigan. We thank Drs. K. Claiborn and members of the Soleimanpour laboratory for helpful advice.

Author Contributions

G.L.P. and E.M.W. conceived, designed and performed experiments, interpreted results, drafted and reviewed the manuscript. N.L. designed and performed experiments, interpreted results, and reviewed the manuscript. A.L., V.S., J.Z., T.S., E.C.R., A.R., K.M., V.S.P., I.X.Z., B.T., D.Z., S.A.D., and L.H. designed and performed experiments and interpreted results. S.C.J.P., P.A., L.Y., B.A.K., L.S.S., and L.S. designed studies, interpreted results, and reviewed the manuscript. M.L.S. designed studies, interpreted results, edited, and reviewed the manuscript. S.A.S. conceived and designed the studies, interpreted results, drafted, edited, and reviewed the manuscript.

Conflict of interest statement

The authors have declared that no conflict of interest exists.

REFERENCES

1 Lowell, B. B. & Shulman, G. I. Mitochondrial dysfunction and type 2 diabetes. *Science* **307**, 384-387 (2005). https://doi.org:10.1126/science.1104343

2 Anello, M. *et al.* Functional and morphological alterations of mitochondria in pancreatic beta cells from type 2 diabetic patients. *Diabetologia* **48**, 282-289 (2005). https://doi.org:10.1007/s00125-004-1627-9

3 Masini, M. *et al.* Ultrastructural alterations of pancreatic beta cells in human diabetes mellitus. *Diabetes Metab Res Rev* **33** (2017). https://doi.org:10.1002/dmrr.2894

4 Stump, C. S., Short, K. R., Bigelow, M. L., Schimke, J. M. & Nair, K. S. Effect of insulin on human skeletal muscle mitochondrial ATP production, protein synthesis, and mRNA transcripts. *Proc Natl Acad Sci U S A* **100**, 7996-8001 (2003). https://doi.org:10.1073/pnas.1332551100

5 Asmann, Y. W. *et al.* Skeletal muscle mitochondrial functions, mitochondrial DNA copy numbers, and gene transcript profiles in type 2 diabetic and nondiabetic subjects at equal levels of low or high insulin and euglycemia. *Diabetes* **55**, 3309-3319 (2006). https://doi.org:10.2337/db05-1230

6 Phielix, E. *et al.* Lower intrinsic ADP-stimulated mitochondrial respiration underlies in vivo mitochondrial dysfunction in muscle of male type 2 diabetic patients. *Diabetes* **57**, 2943-2949 (2008). https://doi.org:10.2337/db08-0391

7 Ritov, V. B. *et al.* Deficiency of subsarcolemmal mitochondria in obesity and type 2 diabetes. *Diabetes* **54**, 8-14 (2005). https://doi.org:10.2337/diabetes.54.1.8

8 Koliaki, C. *et al.* Adaptation of hepatic mitochondrial function in humans with non-alcoholic fatty liver is lost in steatohepatitis. *Cell Metab* **21**, 739-746 (2015). https://doi.org:10.1016/j.cmet.2015.04.004

9 Schmid, A. I. *et al.* Liver ATP synthesis is lower and relates to insulin sensitivity in patients with type 2 diabetes. *Diabetes Care* **34**, 448-453 (2011). https://doi.org:10.2337/dc10-1076

10 Szendroedi, J. *et al.* Abnormal hepatic energy homeostasis in type 2 diabetes. *Hepatology* **50**, 1079-1086 (2009). https://doi.org:10.1002/hep.23093

11 Kotronen, A., Juurinen, L., Tiikkainen, M., Vehkavaara, S. & Yki-Jarvinen, H. Increased liver fat, impaired insulin clearance, and hepatic and adipose tissue insulin resistance in type 2 diabetes. *Gastroenterology* **135**, 122-130 (2008). https://doi.org:10.1053/j.gastro.2008.03.021

12 Pinti, M. V. *et al.* Mitochondrial dysfunction in type 2 diabetes mellitus: an organ-based analysis. *Am J Physiol Endocrinol Metab* **316**, E268-E285 (2019). https://doi.org:10.1152/ajpendo.00314.2018

13 Wigger, L. *et al.* Multi-omics profiling of living human pancreatic islet donors reveals heterogeneous beta cell trajectories towards type 2 diabetes. *Nat Metab* **3**, 1017-1031 (2021). https://doi.org:10.1038/s42255-021-00420-9

14 Koeck, T. *et al.* A common variant in TFB1M is associated with reduced insulin secretion and increased future risk of type 2 diabetes. *Cell Metab* **13**, 80-91 (2011). https://doi.org:10.1016/j.cmet.2010.12.007

15 Sangwung, P., Petersen, K. F., Shulman, G. I. & Knowles, J. W. Mitochondrial Dysfunction, Insulin Resistance, and Potential Genetic Implications. *Endocrinology* **161** (2020). https://doi.org:10.1210/endocr/bqaa017

16 Palmer, C. J. *et al.* Cdkal1, a type 2 diabetes susceptibility gene, regulates mitochondrial function in adipose tissue. *Mol Metab* **6**, 1212-1225 (2017). https://doi.org:10.1016/j.molmet.2017.07.013

17 Kraja, A. T. *et al.* Associations of Mitochondrial and Nuclear Mitochondrial Variants and Genes with Seven Metabolic Traits. *Am J Hum Genet* **104**, 112-138 (2019). https://doi.org:10.1016/j.ajhg.2018.12.001
18 Mercader, J. M. *et al.* Identification of novel type 2 diabetes candidate genes involved in the crosstalk between the mitochondrial and the insulin signaling systems. *PLoS Genet* **8**, e1003046 (2012). https://doi.org:10.1371/journal.pgen.1003046
19 Yonova-Doing, E. *et al.* An atlas of mitochondrial DNA genotype-phenotype associations in the UK Biobank. *Nat Genet* **53**, 982-993 (2021). https://doi.org:10.1038/s41588-021-00868-1
20 Sachdeva, M. M. & Stoffers, D. A. Minireview: Meeting the demand for insulin: molecular mechanisms of adaptive postnatal beta-cell mass expansion. *Mol Endocrinol* **23**, 747-758 (2009). https://doi.org:10.1210/me.2008-0400
21 Cinti, F. *et al.* Evidence of beta-Cell Dedifferentiation in Human Type 2 Diabetes. *J Clin Endocrinol Metab* **101**, 1044-1054 (2016). https://doi.org:10.1210/jc.2015-2860
22 Talchai, C., Xuan, S., Lin, H. V., Sussel, L. & Accili, D. Pancreatic beta cell dedifferentiation as a mechanism of diabetic beta cell failure. *Cell* **150**, 1223-1234 (2012). https://doi.org:10.1016/j.cell.2012.07.029
23 Wang, Z., York, N. W., Nichols, C. G. & Remedi, M. S. Pancreatic beta cell dedifferentiation in diabetes and redifferentiation following insulin therapy. *Cell Metab* **19**, 872-882 (2014). https://doi.org:10.1016/j.cmet.2014.03.010
24 Kahn, C. R., Wang, G. & Lee, K. Y. Altered adipose tissue and adipocyte function in the pathogenesis of metabolic syndrome. *J Clin Invest* **129**, 3990-4000 (2019). https://doi.org:10.1172/JCI129187
25 Moretto, P. *et al.* Regulation of hyaluronan synthesis in vascular diseases and diabetes. *J Diabetes Res* **2015**, 167283 (2015). https://doi.org:10.1155/2015/167283
26 Ikeda, S. *et al.* Yes-Associated Protein (YAP) Facilitates Pressure Overload-Induced Dysfunction in the Diabetic Heart. *JACC Basic Transl Sci* **4**, 611-622 (2019). https://doi.org:10.1016/j.jacbts.2019.05.006
27 Westermann, B. Mitochondrial fusion and fission in cell life and death. *Nat Rev Mol Cell Biol* **11**, 872-884 (2010). https://doi.org:10.1038/nrm3013
28 Kaufman, B. A., Li, C. & Soleimanpour, S. A. Mitochondrial regulation of beta-cell function: maintaining the momentum for insulin release. *Mol Aspects Med* **42**, 91-104 (2015). https://doi.org:10.1016/j.mam.2015.01.004
29 Lawlor, N. *et al.* Single-cell transcriptomes identify human islet cell signatures and reveal cell-type-specific expression changes in type 2 diabetes. *Genome Res* **27**, 208-222 (2017). https://doi.org:10.1101/gr.212720.116
30 Gingerich, M. A. *et al.* An intrinsically disordered protein region encoded by the human disease gene CLEC16A regulates mitophagy. *Autophagy*, 1-19 (2022). https://doi.org:10.1080/15548627.2022.2080383
31 Sidarala, V. *et al.* Mitofusin 1 and 2 regulation of mitochondrial DNA content is a critical determinant of glucose homeostasis. *Nat Commun* **13**, 2340 (2022). https://doi.org:10.1038/s41467-022-29945-7
32 Sidarala, V. *et al.* Mitophagy protects beta cells from inflammatory damage in diabetes. *JCI Insight* **5** (2020). https://doi.org:10.1172/jci.insight.141138
33 Sun, N. *et al.* Measuring In Vivo Mitophagy. *Mol Cell* **60**, 685-696 (2015). https://doi.org:10.1016/j.molcel.2015.10.009
34 Sun, N. *et al.* A fluorescence-based imaging method to measure in vitro and in vivo mitophagy using mt-Keima. *Nat Protoc* **12**, 1576-1587 (2017). https://doi.org:10.1038/nprot.2017.060

35 Soleimanpour, S. A. *et al.* Diabetes Susceptibility Genes Pdx1 and Clec16a Function in a Pathway Regulating Mitophagy in beta-Cells. *Diabetes* **64**, 3475-3484 (2015). https://doi.org:10.2337/db15-0376
36 Gunton, J. E. *et al.* Loss of ARNT/HIF1beta mediates altered gene expression and pancreatic-islet dysfunction in human type 2 diabetes. *Cell* **122**, 337-349 (2005). https://doi.org:10.1016/j.cell.2005.05.027
37 Thorens, B. *et al.* Ins1(Cre) knock-in mice for beta cell-specific gene recombination. *Diabetologia* **58**, 558-565 (2015). https://doi.org:10.1007/s00125-014-3468-5
38 Zhu, M. *et al.* beta cell aging and age-related diabetes. *Aging (Albany NY)* **13**, 7691-7706 (2021). https://doi.org:10.18632/aging.202593
39 Silva, J. P. *et al.* Impaired insulin secretion and beta-cell loss in tissue-specific knockout mice with mitochondrial diabetes. *Nat Genet* **26**, 336-340 (2000). https://doi.org:10.1038/81649
40 Magnuson, M. A. & Osipovich, A. B. Pancreas-specific Cre driver lines and considerations for their prudent use. *Cell Metab* **18**, 9-20 (2013). https://doi.org:10.1016/j.cmet.2013.06.011
41 Madisen, L. *et al.* A robust and high-throughput Cre reporting and characterization system for the whole mouse brain. *Nature neuroscience* **13**, 133-140 (2010). https://doi.org:10.1038/nn.2467
42 Qiu, W. L. *et al.* Deciphering Pancreatic Islet beta Cell and alpha Cell Maturation Pathways and Characteristic Features at the Single-Cell Level. *Cell Metab* **25**, 1194-1205 e1194 (2017). https://doi.org:10.1016/j.cmet.2017.04.003
43 Hua, H. & Sarvetnick, N. Expression of Id1 in adult, regenerating and developing pancreas. *Endocrine* **32**, 280-286 (2007). https://doi.org:10.1007/s12020-008-9036-3
44 Hua, H. *et al.* BMP4 regulates pancreatic progenitor cell expansion through Id2. *J Biol Chem* **281**, 13574-13580 (2006). https://doi.org:10.1074/jbc.M600526200
45 Ghil, S. H., Jeon, Y. J. & Suh-Kim, H. Inhibition of BETA2/NeuroD by Id2. *Exp Mol Med* **34**, 367-373 (2002). https://doi.org:10.1038/emm.2002.52
46 Lorberbaum, D. S. & Sussel, L. A Notch in Time: Spatiotemporal Analysis of Notch Signaling during Pancreas Development. *Dev Cell* **52**, 681-682 (2020). https://doi.org:10.1016/j.devcel.2020.02.018
47 Georgiadou, E. *et al.* Mitofusins Mfn1 and Mfn2 Are Required to Preserve Glucose- but Not Incretin-Stimulated beta-Cell Connectivity and Insulin Secretion. *Diabetes* **71**, 1472-1489 (2022). https://doi.org:10.2337/db21-0800
48 Kim-Muller, J. Y. *et al.* Aldehyde dehydrogenase 1a3 defines a subset of failing pancreatic beta cells in diabetic mice. *Nat Commun* **7**, 12631 (2016). https://doi.org:10.1038/ncomms12631
49 Szklarczyk, D. *et al.* The STRING database in 2021: customizable protein-protein networks, and functional characterization of user-uploaded gene/measurement sets. *Nucleic Acids Res* **49**, D605-D612 (2021). https://doi.org:10.1093/nar/gkaa1074
50 Gauthier, B. R. *et al.* PDX1 deficiency causes mitochondrial dysfunction and defective insulin secretion through TFAM suppression. *Cell Metab* **10**, 110-118 (2009). https://doi.org:10.1016/j.cmet.2009.07.002
51 Quiros, P. M., Mottis, A. & Auwerx, J. Mitonuclear communication in homeostasis and stress. *Nat Rev Mol Cell Biol* **17**, 213-226 (2016). https://doi.org:10.1038/nrm.2016.23
52 Chen, J., Fontes, G., Saxena, G., Poitout, V. & Shalev, A. Lack of TXNIP protects against mitochondria-mediated apoptosis but not against fatty acid-induced ER stress-mediated beta-cell death. *Diabetes* **59**, 440-447 (2010). https://doi.org:10.2337/db09-0949
53 Quiros, P. M. *et al.* Multi-omics analysis identifies ATF4 as a key regulator of the mitochondrial stress response in mammals. *J Cell Biol* **216**, 2027-2045 (2017). https://doi.org:10.1083/jcb.201702058

54 Walker, J. T. *et al.* Integrated human pseudoislet system and microfluidic platform demonstrate differences in GPCR signaling in islet cells. *JCI Insight* **5** (2020). https://doi.org:10.1172/jci.insight.137017
55 Soleimanpour, S. A. *et al.* The diabetes susceptibility gene Clec16a regulates mitophagy. *Cell* **157**, 1577-1590 (2014). https://doi.org:10.1016/j.cell.2014.05.016
56 Pearson, G. *et al.* Clec16a, Nrdp1, and USP8 Form a Ubiquitin-Dependent Tripartite Complex That Regulates beta-Cell Mitophagy. *Diabetes* **67**, 265-277 (2018). https://doi.org:10.2337/db17-0321
57 Heinz, S. *et al.* Simple combinations of lineage-determining transcription factors prime cis-regulatory elements required for macrophage and B cell identities. *Mol Cell* **38**, 576-589 (2010). https://doi.org:10.1016/j.molcel.2010.05.004
58 Gu, C. *et al.* Pancreatic beta cells require NeuroD to achieve and maintain functional maturity. *Cell Metab* **11**, 298-310 (2010). https://doi.org:10.1016/j.cmet.2010.03.006
59 Chen, H., Walker, G. E., Taylor, S. I. & McKeon, C. Proximal enhancer of the human insulin receptor gene binds the transcription factor Sp1. *Diabetes* **43**, 884-889 (1994). https://doi.org:10.2337/diab.43.7.884
60 DHAWAN, S., GURLO, T. & WANG, J. K. 259-OR: Epigenetic Coregulation of Beta-Cell Function and Survival in Postnatal Life. *Diabetes* **69** (2020). https://doi.org:10.2337/db20-259-OR
61 Li, T. *et al.* Multi-stage analysis of gene expression and transcription regulation in C57/B6 mouse liver development. *Genomics* **93**, 235-242 (2009). https://doi.org:10.1016/j.ygeno.2008.10.006
62 Sustarsic, E. G. *et al.* Cardiolipin Synthesis in Brown and Beige Fat Mitochondria Is Essential for Systemic Energy Homeostasis. *Cell Metab* **28**, 159-174 e111 (2018). https://doi.org:10.1016/j.cmet.2018.05.003
63 Teresak, P. *et al.* Regulation of PRKN-independent mitophagy. *Autophagy* **18**, 24-39 (2022). https://doi.org:10.1080/15548627.2021.1888244
64 Claypool, S. M. & Koehler, C. M. The complexity of cardiolipin in health and disease. *Trends Biochem Sci* **37**, 32-41 (2012). https://doi.org:10.1016/j.tibs.2011.09.003
65 Perdikari, A. *et al.* BATLAS: Deconvoluting Brown Adipose Tissue. *Cell Rep* **25**, 784-797 e784 (2018). https://doi.org:10.1016/j.celrep.2018.09.044
66 Ishida, E., Kim-Muller, J. Y. & Accili, D. Pair Feeding, but Not Insulin, Phloridzin, or Rosiglitazone Treatment, Curtails Markers of beta-Cell Dedifferentiation in db/db Mice. *Diabetes* **66**, 2092-2101 (2017). https://doi.org:10.2337/db16-1213
67 Dai, D. F. *et al.* Mitochondrial oxidative stress mediates angiotensin II-induced cardiac hypertrophy and Galphaq overexpression-induced heart failure. *Circulation research* **108**, 837-846 (2011). https://doi.org:10.1161/CIRCRESAHA.110.232306
68 Gurgul, E., Lortz, S., Tiedge, M., Jorns, A. & Lenzen, S. Mitochondrial catalase overexpression protects insulin-producing cells against toxicity of reactive oxygen species and proinflammatory cytokines. *Diabetes* **53**, 2271-2280 (2004). https://doi.org:10.2337/diabetes.53.9.2271
69 Costa-Mattioli, M. & Walter, P. The integrated stress response: From mechanism to disease. *Science* **368** (2020). https://doi.org:10.1126/science.aat5314
70 Halliday, M. *et al.* Partial restoration of protein synthesis rates by the small molecule ISRIB prevents neurodegeneration without pancreatic toxicity. *Cell Death Dis* **6**, e1672 (2015). https://doi.org:10.1038/cddis.2015.49
71 Pagliarini, D. J. *et al.* A mitochondrial protein compendium elucidates complex I disease biology. *Cell* **134**, 112-123 (2008). https://doi.org:10.1016/j.cell.2008.06.016
72 Jazwinski, S. M. The retrograde response: when mitochondrial quality control is not enough. *Biochim Biophys Acta* **1833**, 400-409 (2013). https://doi.org:10.1016/j.bbamcr.2012.02.010

73 Seale, P. *et al.* Transcriptional control of brown fat determination by PRDM16. *Cell Metab* **6**, 38-54 (2007). https://doi.org:10.1016/j.cmet.2007.06.001
74 Uldry, M. *et al.* Complementary action of the PGC-1 coactivators in mitochondrial biogenesis and brown fat differentiation. *Cell Metab* **3**, 333-341 (2006). https://doi.org:10.1016/j.cmet.2006.04.002
75 Jerome, M. S., Kuthethur, R., Kabekkodu, S. P. & Chakrabarty, S. Regulation of mitochondrial function by forkhead transcription factors. *Biochimie* **198**, 96-108 (2022). https://doi.org:10.1016/j.biochi.2022.03.013
76 Vernier, M. & Giguere, V. Aging, senescence and mitochondria: the PGC-1/ERR axis. *J Mol Endocrinol* **66**, R1-R14 (2021). https://doi.org:10.1530/JME-20-0196
77 Yoshihara, E. *et al.* ERRgamma Is Required for the Metabolic Maturation of Therapeutically Functional Glucose-Responsive beta Cells. *Cell Metab* **23**, 622-634 (2016). https://doi.org:10.1016/j.cmet.2016.03.005
78 Liao, X. & Butow, R. A. RTG1 and RTG2: two yeast genes required for a novel path of communication from mitochondria to the nucleus. *Cell* **72**, 61-71 (1993). https://doi.org:10.1016/0092-8674(93)90050-z
79 Liu, Z. & Butow, R. A. A transcriptional switch in the expression of yeast tricarboxylic acid cycle genes in response to a reduction or loss of respiratory function. *Mol Cell Biol* **19**, 6720-6728 (1999). https://doi.org:10.1128/MCB.19.10.6720
80 Liu, Z. & Butow, R. A. Mitochondrial retrograde signaling. *Annu Rev Genet* **40**, 159-185 (2006). https://doi.org:10.1146/annurev.genet.40.110405.090613
81 Shan, J., Fu, L., Balasubramanian, M. N., Anthony, T. & Kilberg, M. S. ATF4-dependent regulation of the JMJD3 gene during amino acid deprivation can be rescued in Atf4-deficient cells by inhibition of deacetylation. *J Biol Chem* **287**, 36393-36403 (2012). https://doi.org:10.1074/jbc.M112.399600
82 Campbell, S. L. & Wellen, K. E. Metabolic Signaling to the Nucleus in Cancer. *Mol Cell* **71**, 398-408 (2018). https://doi.org:10.1016/j.molcel.2018.07.015
83 Zhang, G., Wang, X., Rothermel, B. A., Lavandero, S. & Wang, Z. V. The integrated stress response in ischemic diseases. *Cell Death Differ* **29**, 750-757 (2022). https://doi.org:10.1038/s41418-021-00889-7
84 Shrestha, N., De Franco, E., Arvan, P. & Cnop, M. Pathological beta-Cell Endoplasmic Reticulum Stress in Type 2 Diabetes: Current Evidence. *Front Endocrinol (Lausanne)* **12**, 650158 (2021). https://doi.org:10.3389/fendo.2021.650158
85 Kahn, S. E., Hull, R. L. & Utzschneider, K. M. Mechanisms linking obesity to insulin resistance and type 2 diabetes. *Nature* **444**, 840-846 (2006). https://doi.org:10.1038/nature05482
86 Guo, S. *et al.* Inactivation of specific beta cell transcription factors in type 2 diabetes. *J Clin Invest* **123**, 3305-3316 (2013). https://doi.org:10.1172/JCI65390
87 Corsa, C. A. S. *et al.* The E3 ubiquitin ligase parkin is dispensable for metabolic homeostasis in murine pancreatic beta cells and adipocytes. *J Biol Chem* **294**, 7296-7307 (2019). https://doi.org:10.1074/jbc.RA118.006763
88 Alejandro, E. U. *et al.* Disruption of O-linked N-Acetylglucosamine Signaling Induces ER Stress and beta Cell Failure. *Cell Rep* **13**, 2527-2538 (2015). https://doi.org:10.1016/j.celrep.2015.11.020
89 Belmonte, F. R. *et al.* Digital PCR methods improve detection sensitivity and measurement precision of low abundance mtDNA deletions. *Sci Rep* **6**, 25186 (2016). https://doi.org:10.1038/srep25186
90 Kolesar, J. E., Wang, C. Y., Taguchi, Y. V., Chou, S. H. & Kaufman, B. A. Two-dimensional intact mitochondrial DNA agarose electrophoresis reveals the structural complexity of the mammalian mitochondrial genome. *Nucleic Acids Res* **41**, e58 (2013). https://doi.org:10.1093/nar/gks1324

91 van der Meulen, T. *et al.* Urocortin 3 marks mature human primary and embryonic stem cell-derived pancreatic alpha and beta cells. *PLoS One* **7**, e52181 (2012). https://doi.org:10.1371/journal.pone.0052181
92 Berg, J., Hung, Y. P. & Yellen, G. A genetically encoded fluorescent reporter of ATP:ADP ratio. *Nat Methods* **6**, 161-166 (2009). https://doi.org:10.1038/nmeth.1288
93 Hodson, D. J. *et al.* Incretin-modulated beta cell energetics in intact islets of Langerhans. *Mol Endocrinol* **28**, 860-871 (2014). https://doi.org:10.1210/me.2014-1038
94 Li, H. *et al.* The Sequence Alignment/Map format and SAMtools. *Bioinformatics* **25**, 2078-2079 (2009). https://doi.org:10.1093/bioinformatics/btp352
95 McGinnis, C. S., Murrow, L. M. & Gartner, Z. J. DoubletFinder: Doublet Detection in Single-Cell RNA Sequencing Data Using Artificial Nearest Neighbors. *Cell Syst* **8**, 329-337 e324 (2019). https://doi.org:10.1016/j.cels.2019.03.003
96 Wolock, S. L., Lopez, R. & Klein, A. M. Scrublet: Computational Identification of Cell Doublets in Single-Cell Transcriptomic Data. *Cell Syst* **8**, 281-291 e289 (2019). https://doi.org:10.1016/j.cels.2018.11.005
97 Butler, A., Hoffman, P., Smibert, P., Papalexi, E. & Satija, R. Integrating single-cell transcriptomic data across different conditions, technologies, and species. *Nat Biotechnol* **36**, 411-420 (2018). https://doi.org:10.1038/nbt.4096
98 Yu, G., Wang, L. G., Han, Y. & He, Q. Y. clusterProfiler: an R package for comparing biological themes among gene clusters. *OMICS* **16**, 284-287 (2012). https://doi.org:10.1089/omi.2011.0118
99 Quinlan, A. R. & Hall, I. M. BEDTools: a flexible suite of utilities for comparing genomic features. *Bioinformatics* **26**, 841-842 (2010). https://doi.org:10.1093/bioinformatics/btq033

FIGURE LEGENDS

Figure 1: Mitochondrial quality control is impaired in β-cells in T2D and is required for maintenance of glucose homeostasis and β-cell mass. (A) mtDNA analysis of whole human islets from non-diabetic or T2D donors. *p<0.05 unpaired Mann-Whitney test. (B) Violin plot showing levels of mitochondrially encoded RNA from single β-cell analysis [29] of Non-Diabetic (ND) or T2D human donors. *p<0.05 unpaired Mann-Whitney test. (C) Quantification of FACS showing the % of β-cells (Fluozin-3+) containing MTPhagy+ mitochondria (at least 2500 Fluozin-3+/DAPI- events per sample). p<0.05, ###p<0.001 one-way ANOVA Tukey's multiple comparison post-test. (D) Quantification of FACS showing % of non-β-cells containing MTPhagy+. (E) Expression of Clec16a protein by western blot (WB) in islets isolated from 16-week-old Ctrl or Clec16a^{KO} mice. Vinculin serves as a loading control. (F) Blood glucose concentration measured during an IPGTT of Ctrl (black lines) or β-Clec16a^{KO} (orange lines) mice following 12-weeks regular fat diet (RFD; solid lines) or high fat diet (HFD; dashed lines). n=10-18mice per group, $$$p<0.001 Ctrl RFD vs β-Clec16a^{KO} RFD; $$$$p<0.0001 Ctrl HFD vs β-Clec16a^{KO} HFD by 2-way ANOVA. (G) Serum insulin levels following a 6hr fast. n=12-16 mice per group; **p<0.01, ****p<0.0001 one-way ANOVA, Tukey's multiple comparison post-test. (H) *In vivo* insulin secretion presented as stimulation index. n=12-16 mice per group; ***p<0.001 one-way ANOVA, Tukey's multiple comparison post-test. (I) Pancreatic β-cell mass from 12-week diet fed (16-week-old) Ctrl or β-Clec16a^{KO} mice. n=8-13 mice per group; **p<0.01 one-way ANOVA, Tukey's multiple comparison post-test. (J) β-cell apoptosis measured as the % of TUNEL+/Insulin+ cells. n=4-11 mice per group. (K) Expression of Tfam protein by WB in isolated islets from 10-week-old Ctrl or β-Tfam^{KO} mice. Vinculin serves as a loading control. (L) Quantification of mtDNA (ND4) versus nuclear DNA (Ndufv1) from live FACS sorted islet cells of Ctrl (white bars) or β-Tfam^{KO} (blue bars) mice. n=4 mice per group; ****p<0.0001 one-way ANOVA, Tukey's multiple comparison post-test. (M) Blood glucose concentrations during an IPGTT of Ctrl (black lines) or β-Tfam^{KO} mice at 10-weeks of age. n=8-14 animals per group; $$$$p<0.0001 two-way ANOVA effect of genotype. (N) Serum

insulin measured during *in vivo* glucose-stimulated insulin release in 10-week-old Ctrl (black circles) or β-Tfam^{KO} (blue squares). n=7-8 animals per group; *p<0.05, **p<0.05, ****p<0.0001 one-way ANOVA, Tukey's multiple comparison post-test. (O) Pancreatic β-cell mass from 12-week-old Ctrl (black circles) or β-Tfam^{KO} (blue squares). n=8-13 mice per group; #p<0.05 Student's unpaired t-test. (P) β-cell proliferation measured as the % of Ki67+/Insulin+ cells in 12-week-old mice. n=4 mice per group; ###p<0.001 Student's unpaired t-test. (Q) β-cell apoptosis measured as the % of TUNEL+/Insulin+ cells. n=4-11 mice per group; #p<0.05 Student's unpaired t-test.

Figure 2. Defects in β-cell mitochondrial quality control elicit β-cell immaturity. (A-D) Gene Set Enrichment Analysis (GSEA) of whole islet RNA-Seq from (A) Ctrl versus β-Clec16a^{KO} whole islets or (C) Ctrl versus β-Tfam^{KO}, with heatmaps showing gene expression of a cluster of immature (pink) or mature (blue) genes (gene sets generated from [42]) in (B) Ctrl or β-Clec16a^{KO} islets or (D) Ctrl versus β-Tfam^{KO} whole islets. (E) Heatmap showing expression of core β-cell identity markers from mitophagy (β-Clec16^{KO}) deficient islets. (F) Heatmap showing expression of core β-cell identity markers from β-Tfam^{KO} islets. (G-I) Representative immunofluorescence images for key β-cell dedifferentiation and maturity markers in mitophagy deficient islets (G) Aldh1a3 (red), Pdx1 (green) (H) Glut2 (red), Pdx1 (green) (I) Insulin (green), Pdx1 (red), Ucn3 (blue). (J-K) Representative immunofluorescence images for key β-cell dedifferentiation and maturity markers in β-Tfam^{KO} islets (J) Aldh1a3 (red), Pdx1 (green) (K) Glut2 (red), Pdx1 (green).

Figure 3. Lineage tracing studies implicate regulation of β-cell identity by the mitochondrial quality control pathway. (A-E) Lineage tracing results from Ins1-Cre$^{Rosa26\text{-}tdTomato}$ and β-Clec16a$^{KO\text{-}Rosa26\text{-}tdTomato}$ mice. (A-C) Representative confocal immunofluorescence images showing staining with anti-Insulin (green), anti-Glucagon (blue) and endogenous tdTomato (red). (B-C) magnified images of i, ii, iii white squares. (D) Quantification of Insulin negative tdTomato

positive cells. n=3-6 mice per group; *p<0.05 one-way ANOVA Tukey's multiple comparison post-test. (E) Quantification of Glucagon positive tdTomato positive cells. n=3-6 mice per group. (F-I) Lineage tracing results from Ins1-Cre$^{Rosa26\text{-}tdTomato}$ and β-Tfam$^{KO\text{-}Rosa26\text{-}tdTomato}$ mice. (F-G) Representative confocal immunofluorescence images showing staining with anti-Insulin (green), anti-Glucagon (blue) and endogenous tdTomato (red). (G) magnified images of i, ii, iii white squares. (H) Quantification of Insulin negative tdTomato positive cells. n=3-4 mice per group; ###p<0.001 Student's unpaired t-test. (I) Quantification of Glucagon positive tdTomato positive cells. n=3-4 mice per group; ##p<0.01 Student's unpaired t-test.

Figure 4. Impairments in mitochondrial life cycle activate the mitochondrial integrate stress response (ISR) in rodent and human pseudoislets. (A-D) Comparison analysis of the top 500 upregulated (A) and the top 500 downregulated (B) genes across 3 models of β-cell specific mitochondrial perturbations; mitophagy deficiency (β-Clec16a^{KO}), mtDNA depletion (β-Tfam^{KO}) and fusion deficiency (β-Mfn1/2^{DKO}). (C) STRING analysis of the 62 commonly upregulated and 29 commonly downregulated genes across all models. (D) Expression of pEIF2α (top) and Atf4 (bottom) protein by WB from Ctrl or Clec16^{KO} islets fed RFD or HFD, cyclophilin B serves a loading control. (E) Heatmap generated from bulk RNA sequencing of Ctrl and β-Clec16a^{KO} islets after RFD or HFD showing ISR gene expression. n=4-6 mice per group. (F) Heatmap generated from bulk RNA sequencing of Ctrl and β-Tfam^{KO} islets showing ISR gene expression. n=6-8 mice per group. (G) Bip expression from bulk RNA sequencing of Ctrl or β-Clec16a^{KO} islets after RFD and HFD. n=4-6 mice per group. (H) *Bip* expression from bulk RNA sequencing of Ctrl and β-Tfam^{KO} islets. n=6-8 mice per group. (I) qPCR analysis of *TFAM* and mtRNAs in shScramble or shTFAM expressing human pseudoislets. n=8; *p<0.05, **p<0.001 Student's unpaired t-test (J) TFAM protein expression in shTFAM compared with shScramble pseudoislets. C-peptide marks β cells. Scale bar=50μm, n=4. (K) Expression of pEIF2α, total EIF2α and ATF4 protein by WB from shScramble or shTFAM pseudoislets. Vinculin serves a

loading control. n=3. (L) ISR target genes, BIP expression and (M) β cell markers by qPCR in shScramble or shTFAM pseudoislets. n=4-8; *p<0.05 Student's unpaired t-test.

Figure 5. Loss of mitochondrial quality control induces chromatin remodeling. (A) UMAP plots of snRNA-seq from Ctrl and β-Clec16a^{KO} islet cell nuclei (left) and snATAC-seq (right) from Ctrl and β-Clec16a^{KO} islet cell nuclei. (B) Venn diagram of common and unique open chromatin regions from snATAC-seq of Ctrl and β-Clec16a^{KO} β- cell nuclei. (C) Representative *Ins2* snATAC- and bulk RNA expression-peaks from Ctrl (1st and 3rd tracks) and β-Clec16a^{KO} (2nd and 4th tracks). (D) Representative *Atf3* snATAC- and bulk RNA expression-peaks from Ctrl (1st and 3rd tracks) and β-Clec16a^{KO} (2nd and 4th tracks). (E) HOMER analysis of Ctrl β-Cell ATAC peaks showing enrichment of motifs corresponding to zinc finger (Zf) and beta-Helix Loop Helix (bHLH) identity factors (left) and β-Clec16a^{KO} β-Cell ATAC peaks showing enrichment of motifs corresponding to bZIP stress response factors (right). (F) Visualization of the top 8 enriched TF motifs from Ctrl β-cell specific ATAC peaks (red) and β-Clec16a^{KO} β-cell specific ATAC peaks (blue).

Figure 6. Mitochondrial dysfunction leads to activation of the ISR and induction of immaturity in several metabolic tissues. (A) Schematic of AAV8-Tbg^{cre} delivery and analysis of liver-specific loss of mitochondrial fusion (L-Mfn1/2^{DKO}) and mtDNA (L-Tfam^{KO}). (B) Protein expression of Mfn1 and Mfn2 by WB in Ctrl (AAV8-Tbg^{cre}) and L-Mfn1/2^{DKO} liver. (C) Protein expression of Tfam by WB in Ctrl (AAV8-Tbg^{cre}) and L-Tfam^{KO} liver. (E) Quantification of mtDNA (ND4) to nucDNA (Ndufv1) in liver. n=4-6 animals per group; #p<0.05 one-way ANOVA tukey's multiple comparision post-test. (E) Protein expression of murine oxphos complexes in Ctrl and L-Mfn1/2^{DKO} by WB of liver. Vinculin serves as a loading control. (F) Protein expression of murine oxphos complexes in Ctrl and Tfam^{KO} by WB of liver. Vinculin serves as a loading control. (G) Protein expression of Tom20 in Ctrl and L-Mfn1/2^{DKO} liver by WB. Vinculin serves as a loading

control. (H) Protein expression of Tom20 in Ctrl and L-Tfam^{KO} liver by WB. Vinculin serves as a loading control. (I) Densitometry quantification of oxphos components and Tom20 from (F-G). n=3-6 mice per group; *p<0.05, **p<0.01, ***p<0.001 student's unpaired t-test vs AAV8-Tbg^{cre}. ND=not detected. (J-L) Serum liver function analyses from AAV8-Tbg^{cre} Ctrl (black bars), L-Mfn1/2^{DKO} (green bars) and L-Tfam^{KO}. (J) Serum ALT; ##p<0.01 one-way ANOVA Tukey's multiple comparison post-test. (K) Circulating serum cholesterol levels; #p<0.05 one-way ANOVA Tukey's multiple comparison post-test. (L) Circulating serum LDH levels; #p<0.05 one-way ANOVA Tukey's multiple comparison post-test. (M-N) Differential gene expression comparison plots of AAV-Tbg^{cre} Ctrl vs either L-Tfam^{KO} (y-axis) or L-Mfn1/2^{DKO} (x-axis) showing similarly upregulated ISR genes (M), immature genes [61] (N) and similarly downregulated mature genes [61] (O). (P) Protein expression of pEIF2α (top panels) or Atf4 (bottom panels) in AAV8-Tbg^{cre}, L-Mfn1/2^{DKO} and L-Tfam^{KO} liver. Vinculin and tEIFα serve as loading controls. (Q) Densitometry of pEIF2α and Atf4 protein levels. n=3-6 mice per group; **p<0.01, ****p<0.0001 student's unpaired t-test vs AAV8-Tbg^{cre}. (R) Protein expression of immature (Top2a, AFP and Psat-1) and mature (Mup-3, Cyp2e1) liver markers from AAV8-Tbg^{cre}, L-Mfn1/2^{DKO} and L-Tfam^{KO}. Vinculin serves as a loading control. (S) Densitometry of immature and mature protein levels shown in (R). n=3-6 mice per group; *p<0.05, **p<0.01, ***p<0.001, ****p<0.0001 student's unpaired t-test vs AAV8-Tbg^{cre}. (T) Volcano plot of differential gene expression in Ctrl vs AdCKO (tamoxifen-inducible adiponectin Cre-driven Crsl1 knock-out) brown fat showing upregulated ISR genes (yellow circles) and downregulated maturity genes (pink circles; generated from [65]).

Figure 7. Pharmacologic inhibition of mitochondrial retrograde signaling *in vivo* restores β-cell mass and maturity. (A) Protein expression of pEIF2α, tEIF2α and Aldh1a3 by WB from Ctrl or β-Clec16a^{KO} islets treated *ex vivo* with ISRIB, cyclophilin B was used as a loading control. (B-D) qPCR of Ctrl (white bars) or β-Clec16a^{KO} (orange bars) islets treated *ex vivo* with (triangles) or without (circles) the ISR inhibitor (ISRIB). n=6mice per group; #p<0.05, ###p<0.01 2-way

ANOVA Sidak's multiple comparison posttest effect of drug within genotype for ISR target *Cebpβ* (B) ISR target *Trib3* (C) β-cell maturity marker Ucn3 (D). (E) Ratio of acidic to neutral compartment localized mitochondria from mtKeima-Ctrl (white bars) or mtKeima-β-Clec16a^{KO} (orange bars) treated with (triangles) or without (circles) ISRIB *ex vivo* for 24hr. n=5-7mice per group; $$$$p<0.0001 one-way ANOVA Tukey's multiple comparison post-test. (F) Schematic of *in vivo* ISRIB treatment and analysis of Ctrl or β-Clec16a^{KO} mice. (G-J) Results from Ctrl (white) or β-Clec16a^{KO} mice (orange) treated with daily IP-ISRIB (triangles) or Vehicle (circles) for 4-weeks. n=8-10 mice per group; #p<0.05 2-way ANOVA effect of ISRIB within genotype. *p<0.05 student's unpaired t-test. (G) Blood glucose concentrations during an IP-GTT. (H) AUC calculated from IP-GTT data. (I) Pancreatic β-cell mass. (J) Blood glucose levels during an ITT. (K-M) Representative pancreatic immunofluorescence images from Ctrl or β-Clec16a^{KO} mice treated *in vivo* with Vehicle or ISRIB. (K) Sections stained with antibodies against Aldh1a3 (red), Pdx1 (green), and DAPI (blue). (L) Sections stained with antibodies against Ucn3 (red), Pdx1 (green), and DAPI (blue). (M) Sections stained with antibodies against Glut2 (red) Pdx1 (green), and DAPI (blue). (N-P) Quantification of staining for (N) % cytosolic Aldh1a3^{+} / Pdx1^{+} cells. n=4-5 mice per group; $$p<0.01 one-way ANOVA Tukey's multiple comparison post-test; (O) %Ucn3^{+}/Pdx1^{+} cells. n=5-6 mice/group; $p<0.05, $$$p<0.01 one-way ANOVA Tukey's multiple comparison post-test; and (P) Glut2 localization, classified as all cytosolic (Cytosolic), mixed cytosolic and plasma membrane (Membrane+Cytosolic) and all plasma membrane (Membrane) as a % of all Pdx1^{+} cells. n=6 mice/group; $p<0.05, $$$p<0.01 one-way ANOVA Tukey's multiple comparison post-test (cytosolic localized Glut2).

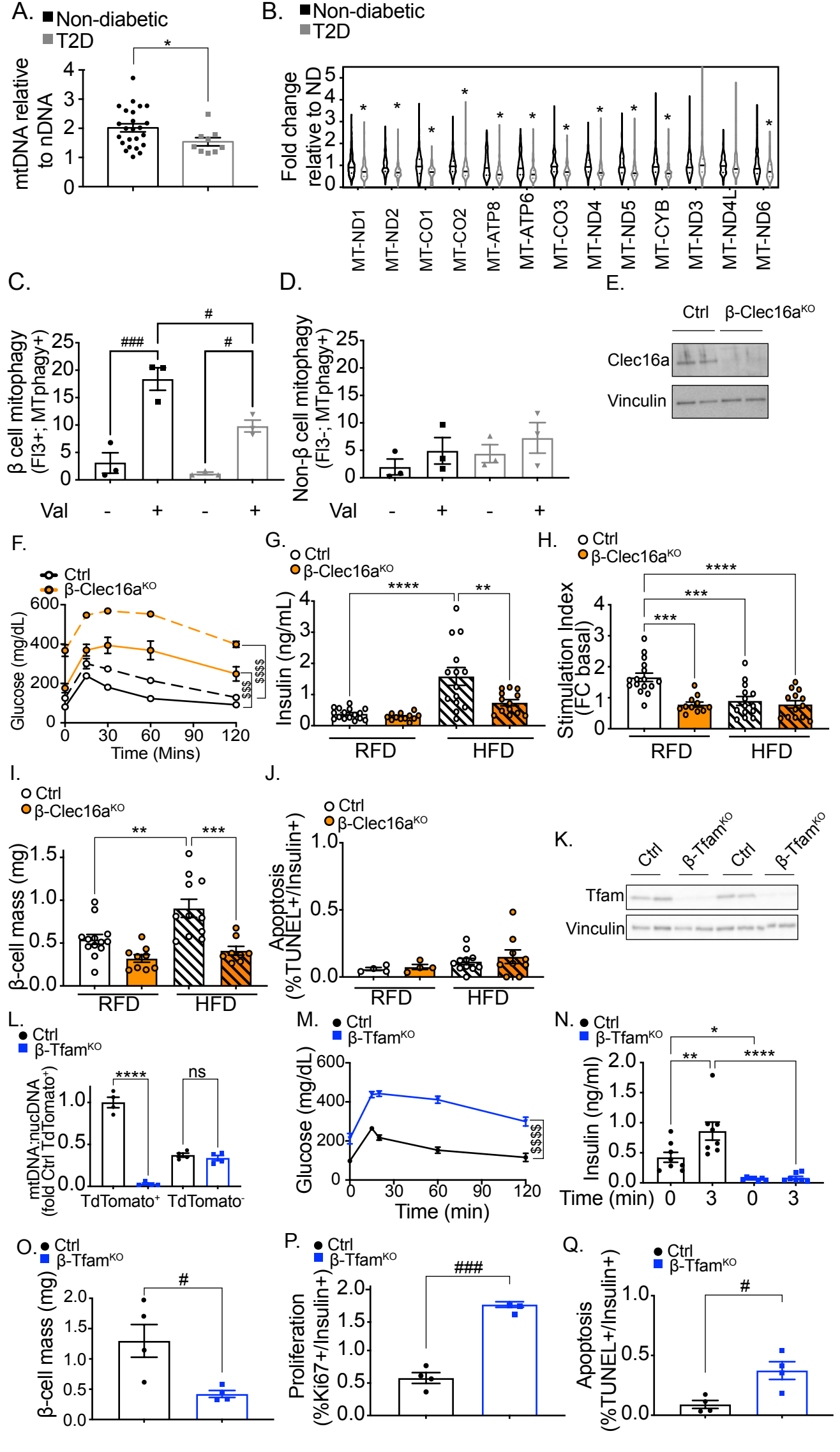
A.
Non-diabetic
T2D
mtDNA relative to nDNA
B.
Non-diabetic
T2D
Fold change relative to ND
MT-ND1
MT-ND2
MT-CO1
MT-CO2
MT-ATP8
MT-ATP6
MT-CO3
MT-ND4
MT-ND5
MT-CYB
MT-ND3
MT-ND4L
MT-ND6
C.
β cell mitophagy (FI3+; MTphagy+)
Val
D.
Non-β cell mitophagy (FI3-; MTphagy+)
Val
E.
Ctrl
β-Clec16a^KO
Clec16a
Vinculin
F.
Ctrl
β-Clec16a^KO
Glucose (mg/dL)
Time (Mins)
G.
Ctrl
β-Clec16a^KO
Insulin (ng/mL)
RFD
HFD
H.
Ctrl
β-Clec16a^KO
Stimulation Index (FC basal)
RFD
HFD
I.
Ctrl
β-Clec16a^KO
β-cell mass (mg)
RFD
HFD
J.
Ctrl
β-Clec16a^KO
Apoptosis (%TUNEL+/Insulin+)
RFD
HFD
K.
Ctrl
β-Tfam^KO
Ctrl
β-Tfam^KO
Tfam
Vinculin
L.
Ctrl
β-Tfam^KO
mtDNA:nucDNA (fold Ctrl TdTomato+)
TdTomato+
TdTomato-
M.
Ctrl
β-Tfam^KO
Glucose (mg/dL)
Time (min)
N.
Ctrl
β-Tfam^KO
Insulin (ng/ml)
Time (min)
O.
Ctrl
β-Tfam^KO
β-cell mass (mg)
P.
Ctrl
β-Tfam^KO
Proliferation (%Ki67+/Insulin+)
Q.
Ctrl
β-Tfam^KO
Apoptosis (%TUNEL+/Insulin+)

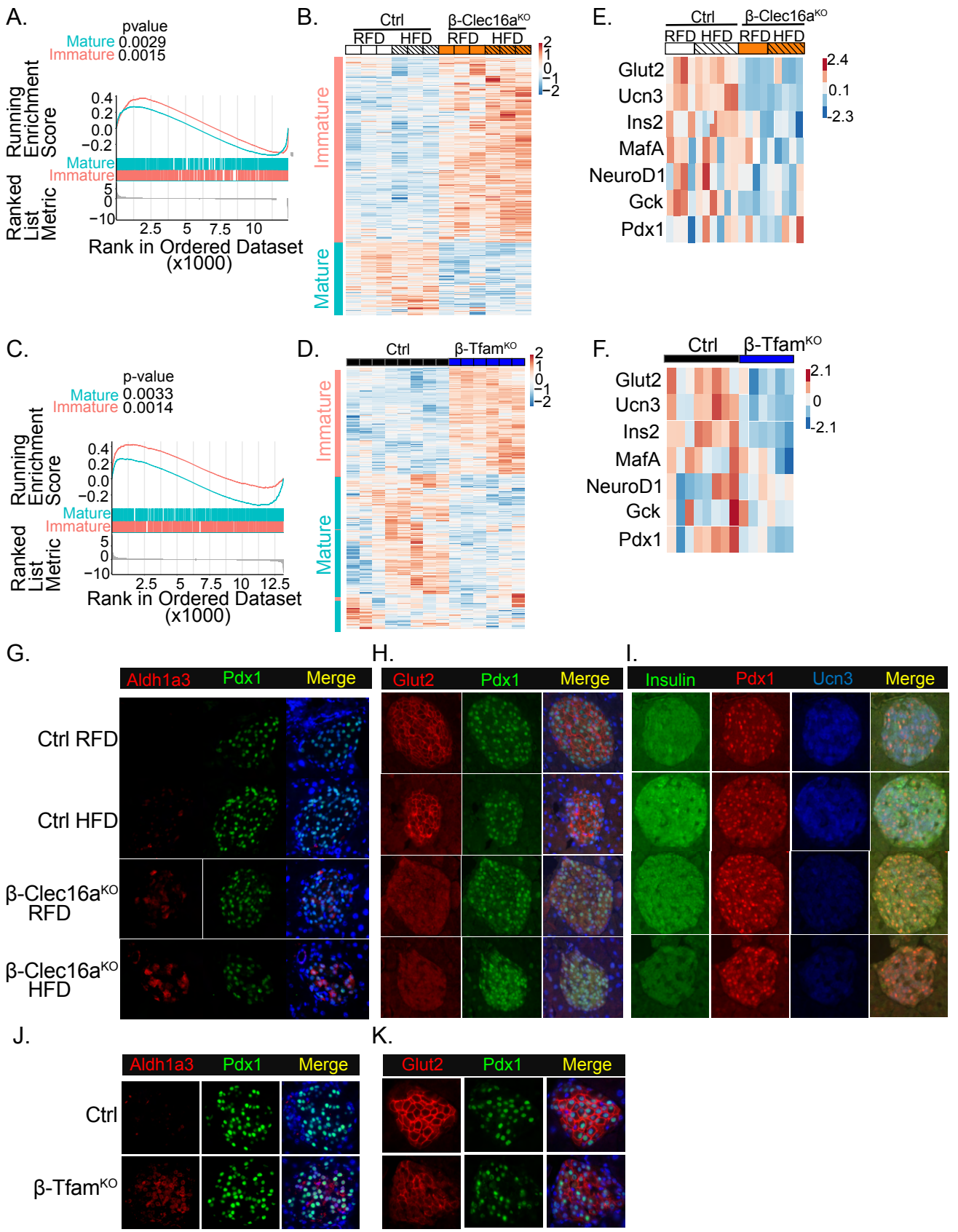
A.
pvalue
Mature 0.0029
Immature 0.0015
Running Enrichment Score
Ranked List Metric
Mature
Immature
Rank in Ordered Dataset (x1000)
B.
Ctrl
β-Clec16a^KO
RFD HFD RFD HFD
Immature
Mature
E.
Ctrl
β-Clec16a^KO
RFD HFD RFD HFD
Glut2
Ucn3
Ins2
MafA
NeuroD1
Gck
Pdx1
C.
p-value
Mature 0.0033
Immature 0.0014
Running Enrichment Score
Ranked List Metric
Mature
Immature
Rank in Ordered Dataset (x1000)
D.
Ctrl
β-Tfam^KO
Immature
Mature
F.
Ctrl
β-Tfam^KO
Glut2
Ucn3
Ins2
MafA
NeuroD1
Gck
Pdx1
G.
Aldh1a3
Pdx1
Merge
Ctrl RFD
Ctrl HFD
β-Clec16a^KO RFD
β-Clec16a^KO HFD
H.
Glut2
Pdx1
Merge
I.
Insulin
Pdx1
Ucn3
Merge
J.
Aldh1a3
Pdx1
Merge
Ctrl
β-Tfam^KO
K.
Glut2
Pdx1
Merge

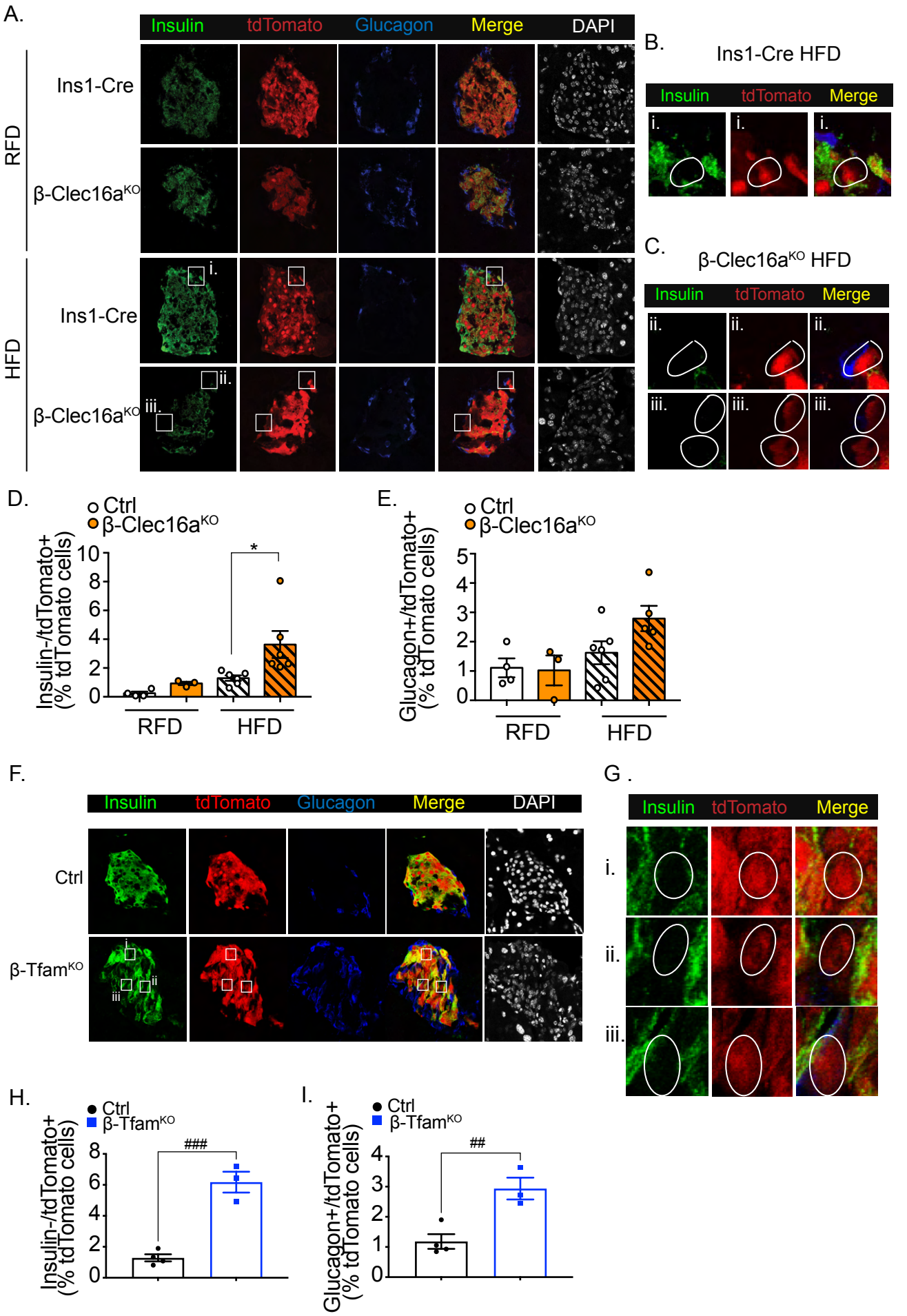
A.
Insulin
tdTomato
Glucagon
Merge
DAPI
RFD
Ins1-Cre
β-Clec16a^KO
HFD
Ins1-Cre
β-Clec16a^KO
i.
ii.
iii.
B.
Ins1-Cre HFD
Insulin
tdTomato
Merge
C.
β-Clec16a^KO HFD
Insulin
tdTomato
Merge
D.
Ctrl
β-Clec16a^KO
Insulin-/tdTomato+ (% tdTomato cells)
RFD
HFD
E.
Ctrl
β-Clec16a^KO
Glucagon+/tdTomato+ (% tdTomato cells)
RFD
HFD
F.
Insulin
tdTomato
Glucagon
Merge
DAPI
Ctrl
β-Tfam^KO
G .
Insulin
tdTomato
Merge
H.
Ctrl
β-Tfam^KO
Insulin-/tdTomato+ (% tdTomato cells)
I.
Ctrl
β-Tfam^KO
Glucagon+/tdTomato+ (% tdTomato cells)

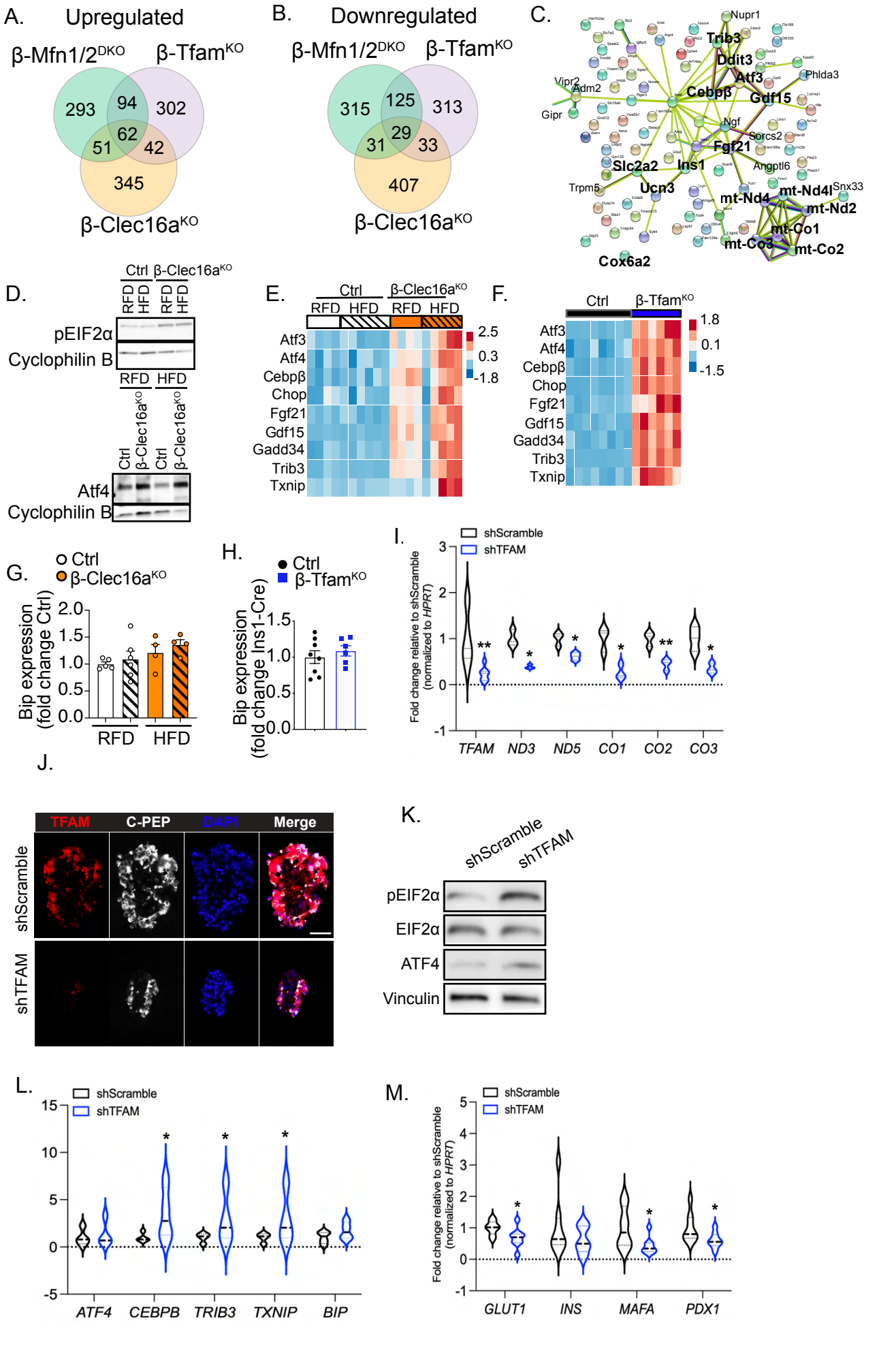
A.
Upregulated
β-Mfn1/2DKO
β-TfamKO
β-Clec16aKO
293
94
302
62
51
42
345
B.
Downregulated
β-Mfn1/2DKO
β-TfamKO
β-Clec16aKO
315
125
313
29
31
33
407
C.
Nupr1
Trib3
Ddit3
Atf3
Phlda3
Vipr2
Adm2
Cebpβ
Gdf15
Gipr
Ngf
Sorcs2
Fgf21
Slc2a2
Ins1
Angptl6
Trpm5
Ucn3
mt-Nd4l
Snx33
mt-Nd4
mt-Nd2
mt-Co1
mt-Co3
mt-Co2
Cox6a2
D.
Ctrl
β-Clec16aKO
RFD
HFD
pEIF2α
Cyclophilin B
Atf4
Cyclophilin B
E.
Ctrl
β-Clec16aKO
RFD
HFD
Atf3
Atf4
Cebpβ
Chop
Fgf21
Gdf15
Gadd34
Trib3
Txnip
2.5
0.3
-1.8
F.
Ctrl
β-TfamKO
1.8
0.1
-1.5
G.
Ctrl
β-Clec16aKO
Bip expression (fold change Ctrl)
RFD
HFD
H.
Ctrl
β-TfamKO
Bip expression (fold change Ins1-Cre)
I.
shScramble
shTFAM
Fold change relative to shScramble (normalized to HPRT)
TFAM
ND3
ND5
CO1
CO2
CO3
J.
TFAM
C-PEP
DAPI
Merge
shScramble
shTFAM
K.
shScramble
shTFAM
pEIF2α
EIF2α
ATF4
Vinculin
L.
shScramble
shTFAM
ATF4
CEBPB
TRIB3
TXNIP
BIP
M.
shScramble
shTFAM
Fold change relative to shScramble (normalized to HPRT)
GLUT1
INS
MAFA
PDX1

A.

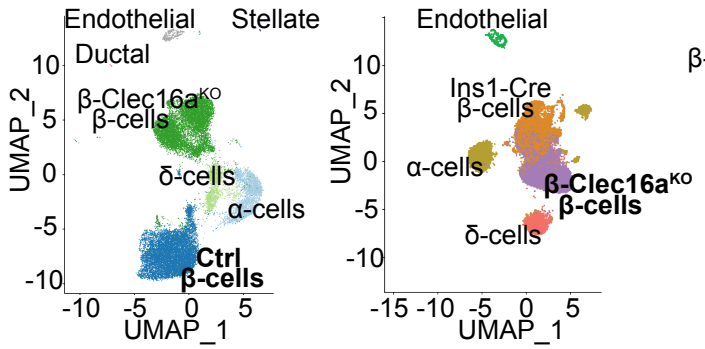

B.

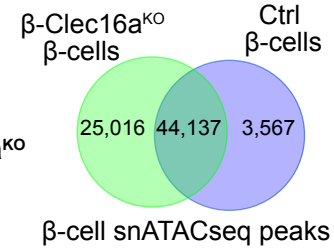

C.

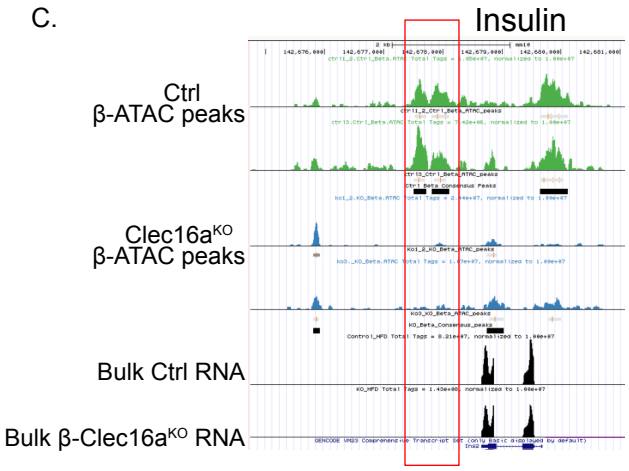

D.

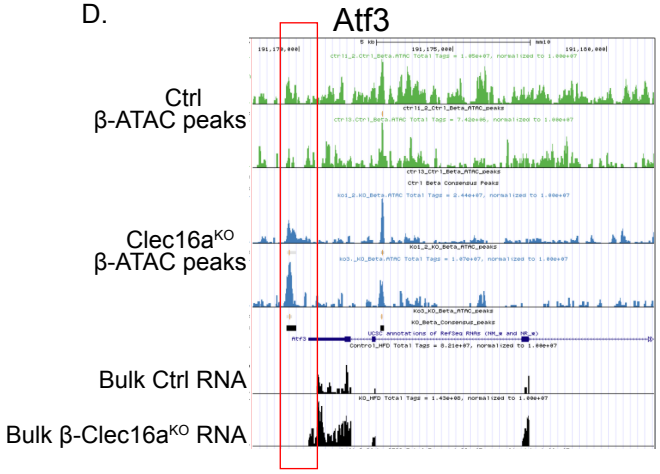

E.

TFs enriched in Ctrl β-cell ATAC peaks

Rank	Motif	Name
1		CTCF(Zf)
2		BORIS(Zf)
3		NeuroD1(bHLH)
4		Atoh1(bHLH)
5		Olig2(bHLH)
6		Ptf1a(HLH)
7		Sp1(Zf)

TFs enriched in β-Clec16a^KO β-cell ATAC peaks

Rank	Motif	Name
1		Chop(bZIP)
2		Atf4(bZIP)
3		BATF(bZIP)
4		Atf3(bZIP)
5		Jun-AP1(bZIP)
6		AP-1(bZIP)
7		CEBP-AP1(bZIP)
8		Bach2(bZIP)

F.

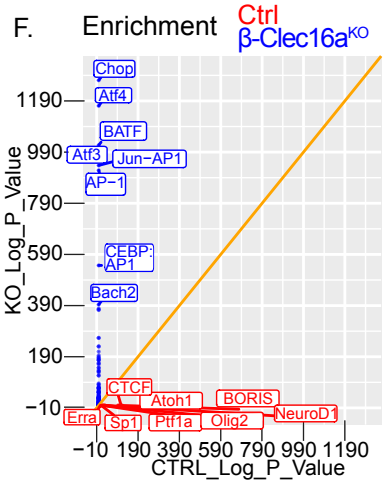

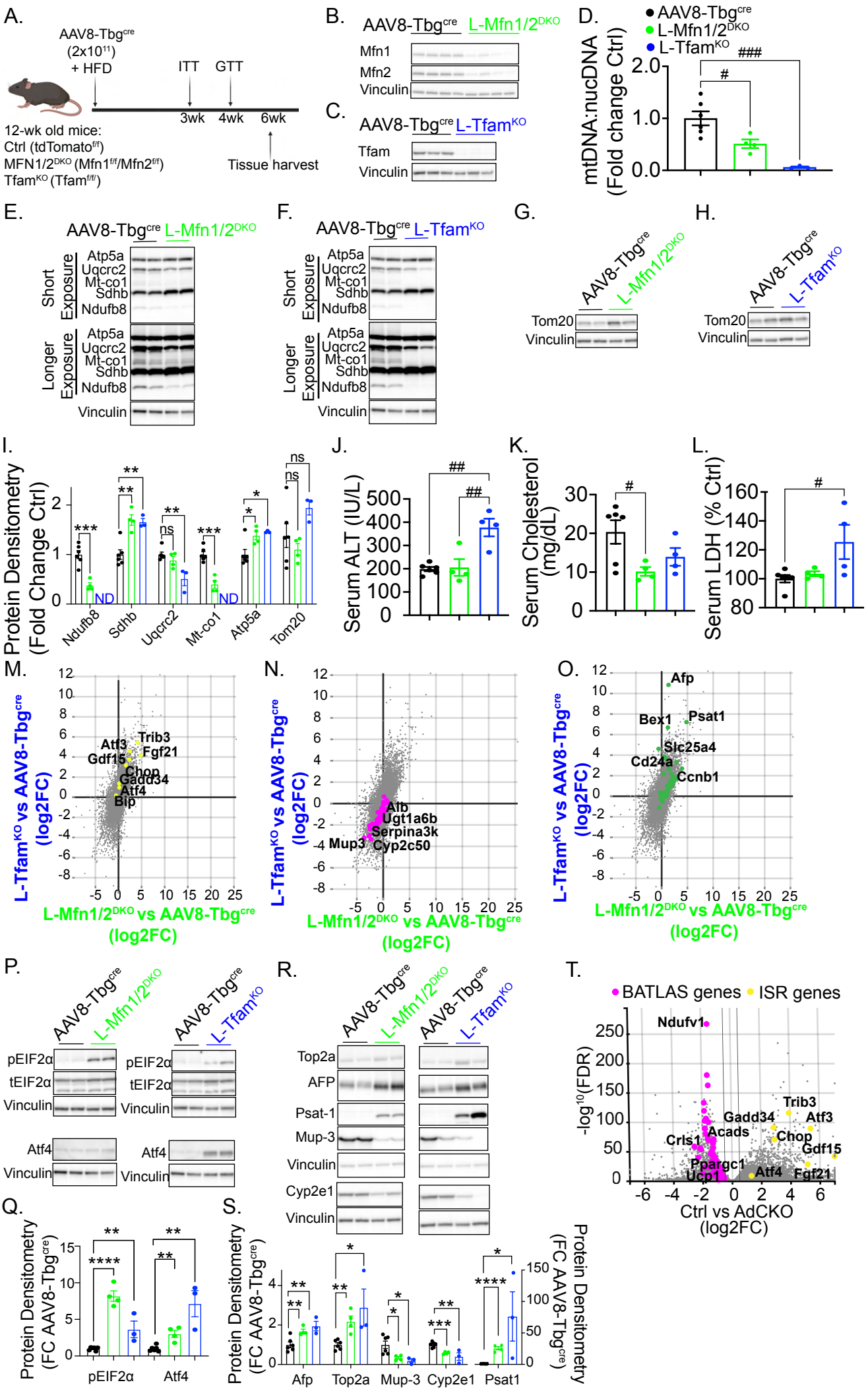
A.
AAV8-Tbg^{cre}
(2x10^{11})
+ HFD
ITT
GTT
3wk
4wk
6wk
Tissue harvest
12-wk old mice:
Ctrl (tdTomato$^{f/f}$)
MFN1/2^{DKO} (Mfn1$^{f/f}$/Mfn2$^{f/f}$)
Tfam^{KO} (Tfam$^{f/f}$)
B.
AAV8-Tbg^{cre}
L-Mfn1/2^{DKO}
Mfn1
Mfn2
Vinculin
C.
AAV8-Tbg^{cre}
L-Tfam^{KO}
Tfam
Vinculin
D.
AAV8-Tbg^{cre}
L-Mfn1/2^{DKO}
L-Tfam^{KO}
mtDNA:nucDNA
(Fold change Ctrl)
E.
AAV8-Tbg^{cre}
L-Mfn1/2^{DKO}
Short Exposure
Longer Exposure
Atp5a
Uqcrc2
Mt-co1
Sdhb
Ndufb8
Vinculin
F.
AAV8-Tbg^{cre}
L-Tfam^{KO}
G.
Tom20
Vinculin
H.
I.
Protein Densitometry
(Fold Change Ctrl)
ND
Ndufb8
Sdhb
Uqcrc2
Mt-co1
Atp5a
Tom20
J.
Serum ALT (IU/L)
K.
Serum Cholesterol
(mg/dL)
L.
Serum LDH (% Ctrl)
M.
L-Tfam^{KO} vs AAV8-Tbg^{cre}
(log2FC)
L-Mfn1/2^{DKO} vs AAV8-Tbg^{cre}
(log2FC)
Atf3
Gdf15
Trib3
Fgf21
Chop
Gadd34
Atf4
Bip
N.
Afb
Ugt1a6b
Serpina3k
Mup3
Cyp2c50
O.
Afp
Bex1
Psat1
Slc25a4
Cd24a
Ccnb1
P.
pEIF2α
tEIF2α
Vinculin
Atf4
R.
Top2a
AFP
Psat-1
Mup-3
Cyp2e1
T.
BATLAS genes
ISR genes
Ndufv1
Trib3
Gadd34
Atf3
Acads
Chop
Crls1
Gdf15
Ppargc1
Ucp1
Atf4
Fgf21
-log^{10}(FDR)
Ctrl vs AdCKO
(log2FC)
Q.
Protein Densitometry
(FC AAV8-Tbg^{cre})
pEIF2α
Atf4
S.
Afp
Top2a
Mup-3
Cyp2e1
Psat1

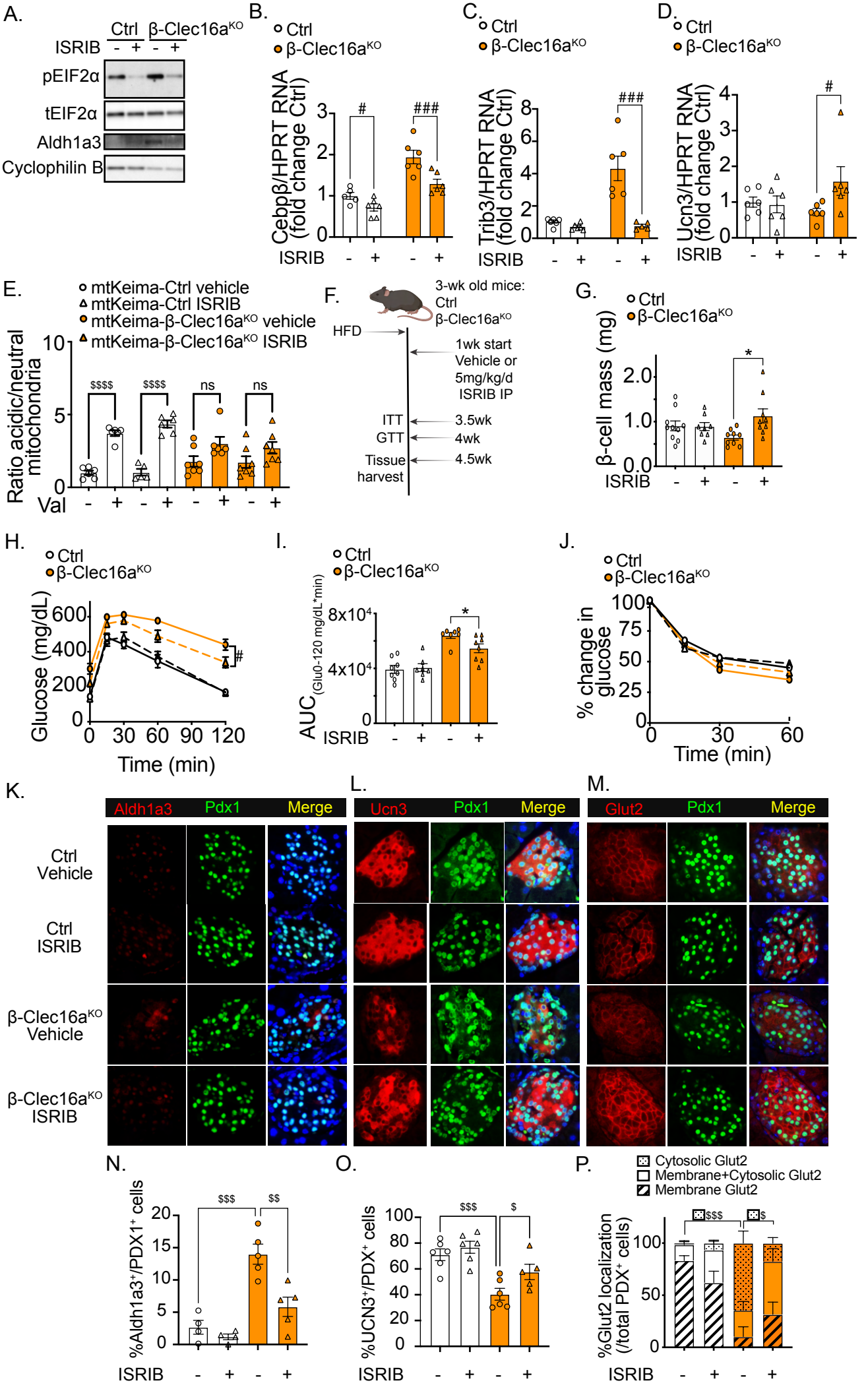
A.
Ctrl
β-Clec16a^KO
ISRIB - + - +
pEIF2α
tEIF2α
Aldh1a3
Cyclophilin B
B.
Ctrl
β-Clec16a^KO
Cebpβ/HPRT RNA (fold change Ctrl)
#
###
ISRIB - + - +
C.
Ctrl
β-Clec16a^KO
Trib3/HPRT RNA (fold change Ctrl)
###
ISRIB - + - +
D.
Ctrl
β-Clec16a^KO
Ucn3/HPRT RNA (fold change Ctrl)
#
ISRIB - + - +
E.
mtKeima-Ctrl vehicle
mtKeima-Ctrl ISRIB
mtKeima-β-Clec16a^KO vehicle
mtKeima-β-Clec16a^KO ISRIB
Ratio acidic/neutral mitochondria
$$$$
$$$$
ns
ns
Val - + - + - + - +
F.
3-wk old mice:
Ctrl
β-Clec16a^KO
HFD
1wk start Vehicle or 5mg/kg/d ISRIB IP
ITT 3.5wk
GTT 4wk
Tissue harvest 4.5wk
G.
Ctrl
β-Clec16a^KO
β-cell mass (mg)
*
ISRIB - + - +
H.
Ctrl
β-Clec16a^KO
Glucose (mg/dL)
#
Time (min)
I.
Ctrl
β-Clec16a^KO
AUC(Glu0-120 mg/dL*min)
*
ISRIB - + - +
J.
Ctrl
β-Clec16a^KO
% change in glucose
Time (min)
K.
Aldh1a3
Pdx1
Merge
Ctrl Vehicle
Ctrl ISRIB
β-Clec16a^KO Vehicle
β-Clec16a^KO ISRIB
L.
Ucn3
Pdx1
Merge
M.
Glut2
Pdx1
Merge
N.
%Aldh1a3+/PDX1+ cells
$$$
$$
ISRIB - + - +
O.
%UCN3+/PDX+ cells
$$$
$
ISRIB - + - +
P.
Cytosolic Glut2
Membrane+Cytosolic Glut2
Membrane Glut2
%Glut2 localization (/total PDX+ cells)
$$$
$
ISRIB - + - +